

Saturn's tropospheric particles phase function and spatial distribution from Cassini ISS 2010-11 observations

Santiago Pérez-Hoyos^{a,b}, José Francisco Sanz-Requena^c, Agustín Sánchez-Lavega^{a,b}, Patrick G.J. Irwin^d, Andrew Smith^d

^a*Departamento de Física Aplicada I, ETS Ingeniería UPV/EHU, Alameda de Urquijo s/n, 48013 Bilbao, Spain*

^b*Unidad Asociada Grupo Ciencias Planetarias UPV/EHU-IAA (CSIC), Bilbao, Spain*

^c*Departamento de Ciencias Experimentales, Universidad Europea Miguel de Cervantes, C/Padre Julio Chevalier, 47012 Valladolid, Spain.*

^d*Atmospheric, Oceanic and Planetary Physics, University of Oxford, Clarendon Laboratory, Parks Road, Oxford OX1 3PU, UK*

Abstract

1 The phase function describes the way particles scatter the incoming radia-
2 tion. This is a fundamental piece of knowledge in order to understand how
3 a planetary atmosphere scatters sunlight and so it has a profound influence
4 in the retrieved atmospheric properties such as cloud height, particle den-
5 sity distribution and radiative forcing by aerosols. In this work we analyze
6 data from the Imaging Science Subsystem (ISS) instrument onboard Cassini
7 spacecraft to determine the particle phase function at blue (451 nm) and
8 near infrared wavelengths (727-890 nm) of particles in the upper troposphere,
9 where most of the incoming visible sunlight is scattered. In order to do so, we
10 use observations taken in later 2010 and 2011 covering a broad range of phase
11 angles from $\sim 10^\circ$ to $\sim 160^\circ$ in the blue (BL1) and near infrared filters as-
12 sociated with intermediate and deep methane absorption bands (MT2, CB2,
13 MT3). Particles at all latitudes are found to be strongly forward scattering.

14 The equatorial particles are in good agreement with laboratory
15 measurements of 10 μm ammonia ice crystals, while mid- and sub-
16 polar latitude particles may be similar to the equatorial particles,
17 but they may also be consistent with 1 μm ellipsoids with mod-
18 erate aspect ratios. Uncertainties due to limited phase coverage
19 and parameter degeneracy prevent strong constraints of the parti-
20 cle shapes and sizes at these locations. Results for the particle phase
21 function are also used to describe the spatial distribution of tropospheric
22 particles both vertically and latitudinally in the Northern hemisphere.

Keywords: Saturn, atmosphere; Radiative transfer; Atmospheres, structure

23 1. Introduction

24 The distribution of aerosols and particles in the upper troposphere and
25 lower stratosphere of the giant planets is a fundamental piece of informa-
26 tion in order to understand the way the atmospheres of these bodies behave.
27 Aerosols act both as scatterers and as absorbers and both roles are essential.
28 By reflecting the incoming sunlight, they serve as tracers for the atmospheric
29 dynamics. These tracers allow the determination of the zonal wind profile
30 (Vasavada et al., 2006; García-Melendo et al., 2011) and its local features
31 (García-Melendo et al., 2010). They also reveal the presence of particular
32 atmospheric structures (del Río-Gaztelurrutia et al., 2010), the most ob-
33 vious ones being the periodic giant storms (often nicknamed Great White
34 Spots, GWS hereafter) arising roughly every seasonal cycle, as seen in 1990
35 (Sánchez-Lavega et al., 1991, 1993) and 2010 (Fischer et al., 2011; Sánchez-
36 Lavega et al., 2011, 2012; Sayanagi et al., 2013). But aerosols forming cloud

37 features do not just serve as passive tracers for the atmospheric dynamics, the
38 combination of their absorption and scattering also has an influence in the
39 energy budget of the planet as reviewed in Pérez-Hoyos and Sánchez-Lavega
40 (2006b). Thus, the goal of this paper is to provide a better understanding of
41 how the Saturnian tropospheric aerosols scatter and absorb solar radiation
42 at visual wavelengths.

43 Briefly speaking, the evolution of our understanding of this topic (i.e.
44 retrieval of vertical distribution of Saturn's upper tropospheric/lower strato-
45 spheric particles by means of reflected sunlight at visible wavelengths) is pro-
46 foundly influenced by the advances in the spacecraft exploring Saturn and
47 their particular orbits. The state of the art by the early 1980s is summarized
48 by the work of Tomasko et al. (1984), in particular the use of methane bands
49 in the near infrared for sounding the planet's atmosphere (West, 1983). Data
50 from Pioneer 11's 1979 flyby of Saturn had provided our first opportunity for
51 measuring the scattering phase function of aerosols in Saturn's atmosphere
52 (Tomasko and Doose, 1984, 1985) at blue ($\sim 440\text{nm}$) and red wavelengths (\sim
53 640nm). The years after the launch of the Hubble Space Telescope provided
54 additional information on general atmospheric properties (Pérez-Hoyos et al.,
55 2005; Karkoschka and Tomasko, 2005) while other ground-based observato-
56 ries (Temma et al., 2005) contributed to the topic. This, together with early
57 work by the Cassini mission, was compiled by West et al. (2009). During the
58 Cassini era, the most notable work on this topic is the study of Roman et al.
59 (2013), which is based in a set of observations very similar to the ones used
60 in this research, although taken some seven years earlier and restricted in
61 phase angle coverage. Obviously, particle properties and related phenomena

62 can also be studied at other wavelengths, e.g. the emitted thermal radiation
63 as in West et al. (2009) or Fletcher et al. (2011a,b), but, all in all, if we want
64 to understand the atmospheric regime as a whole we need to have a good
65 information on where in the atmosphere the particules acting as tracers are
66 located.

67 In spite of the advancement during the last 30 years, particularly due to
68 the use of longer wavelengths to sound levels deeper and higher in the atmo-
69 sphere than those sounded in the visible, the phase function used to describe
70 the way the particles in the upper troposphere scatter incoming radiation is
71 still the one determined by Tomasko and Doose (1984). The prevalence of
72 the Pioneer's phase function is mainly due to the impossibility of observing
73 Saturn at phase angles greater than 6° from Earth. The phase angle is de-
74 fined as the observer-Saturn-Sun angle and supplements the scattering angle.
75 Thus, ground-based observations limited to low phase angles provide infor-
76 mation mostly on the backscattering, while access to the forward scattering
77 requires observations at high phase angles only attainable from spacecraft in
78 orbit around the planet. Since the flybys in the early 1980s, no spacecraft
79 has provided access to this information. During Saturn's seasonal cycle, the
80 characteristic size or shape of the tropospheric particles could have been sub-
81 stantially changed thus modifying the particle phase function. This could in
82 turn result in less accurate vertical cloud structure models and hence, the
83 main goal of this paper is to constrain the particle phase function at least for
84 a snapshot covering Saturn's Northern hemisphere during late 2010 and dur-
85 ing 2011, comparing it with the early work based on Pioneer 11 photometry
86 (Tomasko and Doose, 1984) in 1979. It must be noted that the Pioneer data

87 were restricted to two broad bands, while Cassini ISS allows the use of narrow
88 filters around methane bands which provide a better vertical resolution.

89 The paper is organized as follows: section 2 is devoted to a short descrip-
90 tion of the observations used in this work, as well as to the arguments used
91 for latitude selection. Section 3 covers the radiative transfer model, includ-
92 ing the description for the model atmosphere and its main parameters. The
93 main results are shown in section 4, first presenting the retrieved particle
94 phase function for each latitude, then describing the vertical cloud structure
95 as a function of latitude. A discussion on the meaning of the particle phase
96 function can be found in section 5, as well as the dynamical implications of
97 the retrieved distribution of particles. A summary of the main conclusions
98 of this work is presented in section 6.

99 **2. Observations**

100 *2.1. Overview of the observations*

101 The observations used in this work are summarized in table 1. In this ta-
102 ble, we show the date of each observing run together with the sub-spacecraft
103 planetocentric latitude B (close to the Equator for all cases), the sub-solar
104 planetocentric latitude B' (ranging from 7° N to 12° N) and phase angle α ,
105 defined as explained above as the observer-planet-Sun angle (Sánchez-Lavega,
106 2011). There are 72 images taken in later 2010 and 2011 in a blue wide filter
107 (BL1, 451nm) and three near infrared filters (Porco et al., 2004) which cover
108 an intermediate methane band (MT2, 727nm), its adjacent continuum (CB2,
109 752 nm) and a deep methane band (MT3, 890 nm). The prime criterion for
110 the image selection was to cover a wide range of phase angles for a time

111 short enough not to display evident changes in the apparent reflectivity of
 112 the planet, more than those derived from the changing geometry, as it will be
 113 discussed in section 2.2. This proved to be a challenge, particularly in terms
 114 of latitude coverage, but 2011 offered a good sampling for the above men-
 115 tioned filters for the Northern hemisphere. In the Equatorial Zone (latitudes
 116 below 20°N) the phase angle covers from $\sim 10^\circ$ in August 2011 to $\sim 160^\circ$ in
 117 March 2011, which gives access to scattering angles from $\sim 20^\circ$ to $\sim 170^\circ$.
 118 Mid- and sub-polar latitudes, however, were not observed at this extreme
 119 phase angles and only reach $\sim 110^\circ$, therefore $\sim 70^\circ$ scattering angles. The
 120 same is true for BL1 observations, not including all phase angles. Figures 1
 121 and 2 show cylindrically projected observations for all 18 dates in the three
 122 filters used here.

123 It must be noted that, in December 2010, a GWS erupted in Saturn's
 124 mid-latitudes (Fischer et al., 2011; Sánchez-Lavega et al., 2011), producing an
 125 intense disturbance of the atmosphere in a band roughly covering from 15°N
 126 to 40°N (Sánchez-Lavega et al., 2012; Sayanagi et al., 2013). For an analysis
 127 of the cloud structure of this phenomenon see Sanz-Requena et al. (2012)
 128 and Sromovsky et al. (2013). Obviously, those latitudes were not selectable
 129 for this research and there was a need for checking that the disturbance had
 130 not affected other latitudes.

131 One interesting point for the selected near infrared wavelengths is that
 132 they are close enough not to expect significant variations in the optical prop-
 133 erties (e.g. single scattering albedos, real and imaginary refractive indices
 134 and phase functions), assuming that the spectral behaviour is smooth. So
 135 our first assumption is that particle properties must be constant over the

136 727-890 nm wavelength range. However, methane absorption varies strongly
 137 from one wavelength to another, thus probing a good range of altitudes in the
 138 upper troposphere. The exact sounding levels depend strongly on the vertical
 139 distribution of particles, but for a clear atmosphere they can be calculated
 140 to be between 60 mbar (MT3) down to almost 6 bar (CB2), as shown by
 141 Roman et al. (2013). Since the role of particles is about the same for all the
 142 infrared wavelengths, in a cloudy atmosphere the sounding levels will move
 143 upwards and will tend to squeeze the weighting functions making the aver-
 144 age sounding levels closer in altitude (Sánchez-Lavega et al., 2007). Thus,
 145 the scattering properties are also assumed to be constant over the range of
 146 altitudes sensed by the near infrared filters. Note that this is not necessarily
 147 the case for the BL1 filter observations.

148 All the images were navigated using the PLIA software (Hueso et al.,
 149 2010) and photometrically calibrated to absolute reflectivity using Cassini
 150 Imaging Science Subsystem CALibration software (CISSCAL v3.6) described
 151 by Porco et al. (2004) and West et al. (2010). A full description of the ISS
 152 instrument can be found in fact in Porco et al. (2004). Here we will assume
 153 a constant relative error of 10% in absolute reflectivity for all data. This
 154 number is an intermediate estimate for the dispersion of results retrieved from
 155 observations of standard sources, as discussed in West et al. (2010), where
 156 a more thorough discussion on the sources of uncertainty can be found. In
 157 this work, all observations were transformed into 18 co-registered data cubes
 158 (with two spatial and one spectral directions) oversampled to a resolution of
 159 0.1° per pixel and including scattering angles for each spatial coordinate, as
 160 well as other useful meta data such as date and time of the observations or

161 sub-solar and sub-spacecraft latitude and longitude.

162 *2.2. Reflectivity ratios*

163 We show in figures 1 and 2 the reflectivity maps for all dates used in the
164 following sections. All these maps are Lambert-corrected for limb-darkening,
165 purely for representation purposes. This correction does not work equally
166 well for all filters and latitudes, particularly for BL1 and CB2 observations
167 which are not completely corrected with this approximation. The reflectivity
168 as a function of wavelength and scattering angles is the observable that must
169 be reproduced by the numerical modeling used in this paper; however, the
170 changing geometry makes it difficult to assess the stability of the atmosphere
171 outside the GWS disturbance. Changes in the belt/zone structure of the
172 planets are known to happen with time scales ranging from a few days to
173 some months, apart from the longer scale seasonal cycle (Pérez-Hoyos et al.,
174 2006c).

175 As a first approach to determine whether or not a given latitude has been
176 affected by changes in the overall vertical structure among the 18 dates used
177 in this work, we decided to use the ratio between methane and continuum
178 observations (last column on figures 1 and 2). For a given vertical cloud
179 structure, the ratio between those observations is related to the effective
180 column of methane, which, in the end, is related to the vertical distribution
181 of aerosols. The correlation (or lack of) between methane and continuum
182 observations has been previously discussed, for example, by Roman et al.
183 (2013). This ratio proved to be a valuable tool in order to disentangle the
184 apparent changes from the real ones. For this work, we have computed the
185 ratio of the intermediate methane band filter MT2 to the adjacent continuum

186 CB2. These filters are so close in the spectral range (some 25 nm in central
 187 passband wavelength) that any change in their reflectivity values can be
 188 attributed to differences in methane absorption inside and outside the band.
 189 Higher values of the ratio represent high and thick hazes, such as those in
 190 the Equatorial Zone, while belts displaying thinner and lower haze tops, have
 191 also lower values for the ratio, due to the increased methane absorption due
 192 to a longer atmospheric free path. While using the MT3/CB2 ratio would
 193 have maximized the methane to continuum difference, the MT3 images were
 194 usually acquired with lower spatial resolution (binned for a faster acquisition)
 195 and, moreover, limb-darkening behavior changes too much to be compensated
 196 with those filters even relatively close to the central meridian.

197 *2.3. Latitude selection*

198 In this study we use the MT2/CB2 ratio as a first approach to the overall
 199 distribution of aerosols in the upper troposphere and a similar value of the
 200 ratio is assumed to imply a very similar distribution of such aerosols. It
 201 could be argued that an adequate change in particle phase function or single
 202 scattering albedo could mask a change in the vertical distribution of particles.
 203 However, we find that the zonal mean of the ratio is remarkably stable for
 204 most latitudes (see figure 3) and that the discrepancies are found at the
 205 latitude band identified by morphological and dynamical analyses (Sánchez-
 206 Lavega et al., 2012; Sayanagi et al., 2013).

207 In order to determine the stability of a given latitude, we compute the
 208 standard deviation σ between the zonal means of all dates for the selected
 209 location. Extreme phase angles ($\alpha < 20^\circ$ and $\alpha > 100^\circ$) sometimes divert
 210 from the rest of dates and were removed from this comparison. The differ-

ences for these observations are due to the amplitude of the forward and backscattering peaks of the planetary phase function. In the intermediate range, however, the phase function is apparently flat enough to allow comparisons. As shown in table 1, extreme phase angles are always accompanied by observations at intermediate phase angles in less than a week. This means that only physical changes in time-scales smaller than a week will be overseen with this method. The standard deviation as a function of latitude can be seen in figure 3. It has a constant value of $\sigma \sim 0.012 \pm 0.002$ except in the region between 20°N and 40°N , where it grows strongly. **Additionally, since there were no high phase angle data between 15°N and 20°N , we decided to omit all latitudes between 15°N and 40°N from our analysis and separate the observations into two distinct groups: the Equatorial Zone with latitudes less than 15°N and extended phase coverage, and a mid-latitude regions with latitudes between 40°N and 70°N and more limited phase coverage.**

The Equatorial Zone (EZ, latitudes less than 15°N) has the highest haze tops in the whole planet, as it has already been noted in the past (Pérez-Hoyos and Sánchez-Lavega, 2006a). This region is very interesting dynamically, not only because of the strong vertical wind shear revealed by Hubble Space Telescope data (Sánchez-Lavega et al., 2003) but also because of a strong jet detected at high altitudes through Cassini ISS data, e.g. García-Melendo et al. (2010). Tomasko and Doose (1984) investigated corresponding southern latitudes roughly one Saturnian year earlier and thus this is a very interesting place for a direct comparison with their results.

In contrast, the mid-latitude zone is surrounded by two darker belts;

the poleward belt borders the subpolar latitudes, where high altitude hazes may exhibit different particle properties (Karkoschka and Tomasko, 2005). At mid-latitudes the hazes are known to change in reflectivity from summer to winter, revealing changes in the overlying vertical cloud structure (Karkoschka and Tomasko, 2005). The Cassini observations used in the present study represent a snapshot of the northern hemisphere at spring equinox.

The initial latitude grid for modelling was arbitrarily sampled every 0.5° in latitude. For every date and latitude, we selected 5 points uniformly distributed along the longitudes with illumination and observation angles below 85° at each wavelength to be fit by our radiative transfer code.

3. Radiative transfer model

3.1. Model atmosphere

As in our previous works (Pérez-Hoyos et al., 2005; Sanz-Requena et al., 2012), Saturn’s atmosphere was initially considered to be divided into three distinct layers of particles. Figure 4 shows a simple scheme of this distribution. The top layer is located in the stratosphere and its bottom level, P_2 , is arbitrarily fixed at 100 mbar, a mean value for the tropopause level. Initial tests showed no strong sensitivity to the P_2 value, except for its effect on the total optical thickness of the layer. Particles are assumed to be spherical with their radius being one of the free parameters of the model. They are therefore described using a Mie phase function with the parameters presented in Table 2. In this table, m_r and m_i are, respectively, the real and imaginary parts of the refractive index, assumed to be that of

260 the ammonia ice (Martonchik et al., 1984) but again with little sensitivity
 261 for this assumption. The size distribution is log-normal (Hansen and Travis,
 262 1974) with mean radius r_g and variance σ_g . Particle number density N_1 is
 263 considered constant between P_1 and $P_2 = 100\text{mbar}$ (i.e. with a mixing ratio
 264 increasing with height), but it decays exponentially above P_1 with a scale
 265 height H_1 to be retrieved by the model.

266 The second, intermediate layer is where most of the photons at the wave-
 267 lengths used here are scattered to the observer. This layer was assumed
 268 to be located from somewhere around the tropopause (P_3) down to a place
 269 between the radiative-convective level and the expected condensation cloud
 270 at 1.4bar, here fixed to be at $P_4 = 1\text{bar}$. Most of the filters used here are
 271 not sensitive to this depth, and thus reaching the bottom of the haze **and**
 272 **thus the data are only weakly sensitive to altitude though strongly**
 273 **sensitive to total optical thickness of the layer**. Please note that it is
 274 certainly possible that both hazes overlap. NEMESIS is able to manage over-
 275 lapping particle layers, so no constraints have **been** imposed on the limits of
 276 the hazes.

277 The phase function used for this layer is a double Henyey-Greenstein
 278 parameterized phase function (Henyey and Greenstein, 1941) as in Tomasko
 279 and Doose (1984). This phase function can be written as:

$$P(\theta) = f \cdot \frac{1 - g_1^2}{[1 + g_1^2 - 2g_1\cos(\theta)]^{3/2}} + (1 - f) \cdot \frac{1 - g_2^2}{[1 + g_2^2 - 2g_2\cos(\theta)]^{3/2}} \quad (1)$$

280 In this expression, θ is the scattering angle and $P(\theta)$ the phase function.
 281 This two-term Henyey-Greenstein phase function (2HG) is composed of two
 282 terms with two asymmetry parameters g_1 and g_2 . The first one is usually pos-

283 itive and therefore represents the forward scattering. The second one is, in-
 284 stead, used to describe the backward scattering, while parameter f accounts
 285 for the relative weighting between them. In the radiative transfer equation
 286 written for a plane-parallel atmosphere (Liou, 1992; Sánchez-Lavega, 2011)
 287 the normalized phase function is multiplied by the single scattering albedo
 288 ϖ_0 . This parameter is the ratio of the particle absorption relative to the
 289 particle scattering and perfect absorbers have therefore $\varpi_0 = 0.0$ and perfect
 290 scatterers $\varpi_0 = 1.0$. Highly reflective particles at longer wavelengths are
 291 commonly assumed (Pérez-Hoyos et al., 2005) since no evidence of particle
 292 absorption has been reported. It must be noted that in order to translate
 293 to particle number density to optical thickness, a particle cross section is
 294 required. We assumed **a particle radius of $1\mu\text{m}$ with geometric cross**
 295 **section of $\pi \times 10^{-8}\text{cm}^2$ for the tropospheric particles at all latitudes.**
 296 Retrievals are sensitive to optical thickness or extinction, e.g. particle num-
 297 ber density is only as reliable as our estimation of the cross section is. N_2
 298 could be off if the actual particle cross section is different from the value
 299 assumed here, but the product of both (τ_{trop}) can still be robustly retrieved.

300 As in the previous case, this haze is delimited by top P_3 and bottom P_4
 301 pressures, with the latter fixed to $P_4 = 1\text{bar}$. Again, the particle number
 302 density N_2 is free but constant in this interval and set to decay with a free
 303 scale height H_2 , independent of that of the stratospheric haze.

304 Finally, a cloud deck was also placed from the bottom of the previous
 305 layer ($P_5 = 1\text{bar}$) to the expected ammonia condensation level ($P_6 = 1.4\text{bar}$).
 306 Although initial tests did not show a significant sensitivity, the particle num-
 307 ber density N_3 was used as the main free parameter of this cloud. We as-

308 sumed an isotropic phase function with a fixed single scattering albedo of
 309 $\varpi_0 = 0.995$ (Pérez-Hoyos et al., 2005), and the cross section of $10\ \mu\text{m}$ par-
 310 ticles ($\pi \times 10^{-6}\text{cm}^2$), see West et al. (2009) and references therein. The
 311 assumption of an isotropic phase function has no influence on the results, as
 312 we tested running the forward model with alternative phase functions (double
 313 Henyey-Greenstein and Mie phase function with arbitrary values).

314 In order to complete the vertical cloud structure model the gas behavior
 315 also has to be defined. Our atmosphere is simply described by a mixture
 316 of H_2 and He that produces Rayleigh scattering, although this effect is only
 317 substantial at the shortest wavelengths covered here (BL1), where τ_{Rayleigh}
 318 $= 0.559$ at 1 bar. The other active species is methane, whose volume mixing
 319 ratio has been taken as 4.7×10^{-3} , relative to H_2 (Fletcher et al., 2009). In or-
 320 der to calculate the absorption coefficient of methane we used the coefficients
 321 published by Karkoschka and Tomasko (2010). The pressure-temperature
 322 profile has little influence on the calculated absorption coefficient and that
 323 from Lindal et al. (1985) was used.

324 3.2. Radiative transfer code

325 The radiative transfer code used for this work is NEMESIS. NEMESIS
 326 stands from Non-linear optimal Estimator for MultivariatE spectral analy-
 327 SIS and was developed by the Oxford team (Irwin et al., 2008). It uses an
 328 optimal estimator technique (Rodgers, 2000) in order to perform multivari-
 329 ate retrievals of atmospheric properties from thermal or reflected radiation
 330 from the planets. It has become by now a standard code for radiative trans-
 331 fer in planetary atmospheres. Here, the code is used essentially as a for-
 332 ward model. The correlated-k method version of NEMESIS was used, based

333 in the methane absorption coefficients by Karkoschka and Tomasko (2010).
334 NEMESIS assumes a plane-parallel atmosphere for scattering and it uses a
335 doubling/adding scheme (Hansen and Travis, 1974).

336 Table 2 summarizes the atmospheric model parameters and the range
337 of their values used to start the radiative transfer model. Many of these
338 parameters, such as particle size or phase function parameters, cannot be
339 treated as free parameters in the version of NEMESIS code used here, so
340 we opted for a different approach that will be explained in the next section.
341 This limitation has been removed in more recent versions of the code (Irwin
342 et al., 2015).

343 *3.3. Optimization and retrieval*

344 Table 2 shows the 12 free parameters that should be constrained for every
345 0.5° in latitude by comparing the model results with the observations. This is
346 a huge computational effort that cannot be solved by a brute force approach
347 in a reasonable amount of time. NEMESIS could constrain efficiently some
348 of the parameters (e.g. those referring the vertical distribution of particles)
349 but this would leave others aside, in particular those regarding the particle
350 phase function. This would create a hierarchy between free parameters and,
351 after several initial runs, we realized that all parameters should be treated
352 equally and fitted at the same time. Thus NEMESIS is used here as a forward
353 model, rather than as an optimization suite.

354 Finding the best-fitting model for each case was prioritized over fully
355 sampling the 12-dimensional free parameter space to completely describe the
356 a posteriori space. For doing so, a simplex method (Nelder & Mead, 1965)
357 was used to minimize the error function, described as the mean quadratic

358 deviation χ^2 between data and models, as in many of our previous works (e.g.
 359 Pérez-Hoyos et al. (2012)). This is a reduced χ^2 , an average of all the filters
 360 and positions over the disk being modelled. The simplex method iterates
 361 over a N -dimensional space (the logarithm of each free parameter, to avoid
 362 negative values and scale problems) and it evaluates the function in $N + 1$
 363 points (a simplex), substituting one of the vertices in each iteration. Iteration
 364 is terminated when certain conditions are met. In our case the termination
 365 condition was that $\chi_i^2 - \chi_{i+1}^2 < 10^{-3}$, i.e. that the mean quadratic deviation
 366 did not get better than a thousandth with respect to previous iteration. This
 367 resulted in some 500 iterations for each case.

368 For every latitude, 10 initial models were randomly determined and were
 369 let to evolve until convergence, thus resulting in some 5,000 models ran for
 370 every latitude. Note that no termination condition over the absolute value
 371 of χ^2 was imposed, so the value assumed for relative error σ was of little
 372 importance. The model with minimum χ^2 was selected as the best-fitting
 373 case. We show in Table 2 the initial range for initialization of every fitting
 374 run.

375 3.4. *Sensitivity to model parameters*

376 The large number of models run allows us to perform a statistical analysis
 377 for the sensitivity of the model to the parameters. Since the simplex method
 378 iterates many more times closer to the optimal solution, the most frequent
 379 values of a given parameter are also those with lower values of χ^2 . We can
 380 increase this effect by weighting the frequency by the probability of the model
 381 of being correct. For the most simple case of a problem with a single degree of
 382 freedom, the probability of a given model of being true (as opposed to being

383 similar to observations just by chance) can be defined following de Kleer et
 384 al. (2015), where $\ln P \propto -\chi^2/2$. Since we have used the reduced χ^2 for model
 385 evaluation, we will explore model sensitivity scaling the frequency of a given
 386 parameter by $e^{-\chi^2/2}$. This provides a sampling of the free parameter space
 387 and good information on how the best solutions are distributed in it. Figure
 388 5 shows an example of the exploration of the free parameter space. The
 389 best sensitivity is shown as sharp maximums in the histograms (e.g. as in
 390 N_2 , P_3 or ϖ_0), while low sensitivity is demonstrated by flat or multi-modal
 391 histograms (e.g. as in scale heights H_1 and H_2 or N_3). The sensitivity is
 392 good for f and g_1 parameters of the phase function, but g_2 is shown to have
 393 a broad distribution and therefore our sensitivity to this parameter is going
 394 to be lower.

395 Although the number of models explored and their distribution in the
 396 free parameter space is not optimal for this purpose, we can try to map the
 397 degeneracies between parameters as shown in figure 6, where some combina-
 398 tions of free parameters are displayed. There are some obvious degeneracies
 399 in the distribution of tropospheric particles, such as N_2 and P_3 or N_2 and
 400 H_2 which show that an adequate change in both parameters simultaneously
 401 could provide a model marginally as good as the best one. In the case of the
 402 phase function parameters, g_2 is in particular harder to determine because
 403 the backscattering can be produced by the combination of other parameters
 404 and thus it is not well constrained by our method. However, these results
 405 must be taken with caution and other methods which are statistically better
 406 founded should be used (de Kleer et al., 2015) at the cost of a much higher
 407 computational effort.

408 In order to determine the error bars for every parameter retrieval, we used
 409 a similar approach as in Pérez-Hoyos et al. (2012), rather than being based on
 410 the average statistics shown in figure 5 and 6. Once we have determined the
 411 optimal model within the framework described in the previous paragraphs,
 412 we scan the free parameter space at one dimension each time, thus analysing
 413 the one-dimensional dependence of χ^2 with every parameter. We arbitrarily
 414 defined error bars when the value of χ^2 is twice that of the minimum. This
 415 relative criterion avoided having lower error bars when error is closer to the
 416 absolute limit (typically $\chi^2 = 1$ or something similar). Still, the error bars
 417 retrieved in this way were not very different from those estimated from the
 418 width of histograms described in the previous paragraph and are in good
 419 agreement with the dispersion of values for similar latitudes, as it will be
 420 shown in section 4.

421 **4. Results**

422 *4.1. General results*

423 Using the techniques described in the preceding section, we are able to
 424 fit simultaneously the center to limb scans at the four filters for the 18 cases
 425 in Table 1. The value of the reduced χ^2 for all latitudes is shown in figure
 426 7. Most fits are around $\chi^2 = 1$, which is acceptable. Some example fits are
 427 shown in figures 8 and 9 for two selected latitudes not particularly good or
 428 bad.

429 As it will be discussed later, there is a clear dependence of most param-
 430 eters with latitude, both in their vertical distribution and in their scattering
 431 properties (phase function). In particular, there is a clear difference between

the Equatorial atmosphere and those latitudes above the band disturbed by the storm. It is even possible to distinguish between the purely mid-latitudes (up to some 55°N) and the region polewards of this. However, there are less data for these sub-polar latitudes and observation/illumination angles are more restricted, which results in a higher dispersion of the results. The sub-polar and polar latitudes will be analysed elsewhere using better suited observations.

4.2. *Uncertainties and limitations*

The error bars are substantially different depending on the free parameter, and they are in good agreement with the dispersion of the values in the same latitude region. Results concerning the vertical distribution of tropospheric aerosols are the best-constrained ones with relative errors around 5% for P_3 and 20% for N_2 and H_2 . The stratospheric haze, instead, yields relative errors that exceed 100% for most latitudes and free parameters and thus only help, in the best case, to provide upper/lower limits. Only the radius of stratospheric particles can be constrained occasionally with error bars around 10%. The parameters of the phase function of the tropospheric particles, which are the main goal of this paper, can be commonly retrieved with uncertainties lower than 20%, although the dispersion of results for similar latitudes are usually below that benchmark. The single scattering albedo of the particles is a very sensitive parameter that is usually determined better than 10%.

As seen in figures 8 and 9, most of the model deviation from data is **contributed by** MT2 simulations at high emission angles. The points with emission angles higher than 70° concentrate most of the error and are re-

457 sponsible for the **increased** values of χ^2 . However, this only happens with
 458 at MT2 wavelengths and thus can hardly be attributed to a problem with
 459 the plane parallel approximation. In order to understand the origin of such
 460 discrepancies, we ran three new retrievals for a few latitudes starting from
 461 the best-fitting model already obtained. For these calculations we used three
 462 different approaches: (1) We fit MT2 data at all phase angles simultaneously
 463 but regardless of the results at the other wavelengths; (2) We fit only low
 464 phase angles, but at all filters simultaneously; and (3) Same as (2) but for
 465 an intermediate phase angle $\alpha = 80^\circ$.

466 The first approach tends to reduce the stratospheric haze optical thick-
 467 ness, or even remove it completely ($N_1 \rightarrow 0$). For mid-latitudes with initially
 468 less particles in the levels above 100 mbar, the model tends to change the
 469 scale height of the tropospheric haze H_2 . This way, $\chi^2(MT2)$ is reduced
 470 in a factor of 2 at the cost of increasing the error at other wavelengths, in
 471 particular at MT3, where it can be increased by factor of 10.

472 When we try to fit a single phase angle, either at low or intermediate
 473 phase angles, but all wavelengths at the same time, we also have better fits
 474 than the ones used here. Changes around 25% in N_2 and P_3 are usually
 475 enough to reduce the reduced χ^2 in a factor of 1.5. **While f and g_1 are**
 476 **essentially the same,** backscattering parameter g_2 is also altered by about
 477 10% when studying a low phase angle alone. However, we were not able to
 478 find any better model at low and high phase angles simultaneously.

479 All in all, our model works well at low and intermediate emission angles
 480 but it is just fair for emission angles above 70° , particularly at MT2. Our
 481 analysis above implies that the description of the particle distribution at 10s

482 of mbar, **around the top of the tropospheric haze**, could be improved
 483 with a more sophisticated distribution or with a better vertical resolution.
 484 However, it must be noted that results for phase function parameters are still
 485 robust and within the retrieved error bars.

486 *4.3. Phase function*

487 As shown in figure 10, the results for the phase function show at least
 488 two distinct regions of the planet. While the weighting between the forward
 489 and the backward backscattering is almost the same all over the planet, the
 490 backward and forward parameters change abruptly somewhere between the
 491 Equatorial Zone and the mid-latitudes.

492 Considering all latitudes, the average value for all wavelengths of f is
 493 0.85 ± 0.06 . This is slightly smaller in the EZ ($f = 0.79 \pm 0.04$) than at mid-
 494 latitudes ($f = 0.88 \pm 0.04$), almost within retrieval error bars. Parameter
 495 g_1 changes from $g_1 = 0.75 \pm 0.09$ for latitudes close to the Equator to $g_1 =$
 496 0.83 ± 0.04 for latitudes poleward of the region disturbed by the 2010 giant
 497 storm (GWS). Parameter g_2 is more stable, ranging from $g_2 = -0.33 \pm 0.05$
 498 at the EZ to $g_2 = -0.31 \pm 0.07$. The global averages for both parameters
 499 are $g_1 = 0.81 \pm 0.07$ and $g_2 = -0.31 \pm 0.07$.

500 We tried to get better fits by leaving free the parameters of the 2HG
 501 phase function for the blue wavelengths. However, these observations are
 502 very sensitive to the single scattering albedo and they do not provide any
 503 significant changes in f , g_1 or g_2 . However, the single scattering albedo
 504 $\varpi_0(BL1)$ can be easily constrained and provides values clearly below those
 505 used at NIR wavelengths. Figure 11 shows its value as a function of latitude.
 506 Once again, there is a clear distinction between the Equatorial aerosols and

507 those located at higher latitudes. Mean values are $\varpi_0(BL1) = 0.94 \pm 0.02$,
 508 but this is $\varpi_0(BL1) = 0.92 \pm 0.01$ for EZ and $\varpi_0(BL1) = 0.95 \pm 0.01$ for the
 509 rest of latitudes.

510 4.4. *Spatial distribution*

511 The main results for the parameters regarding the stratospheric haze
 512 are shown in figure 12. However, our model is not very sensitive to these
 513 parameters, in particular because the total integrated optical thickness is
 514 low, with average values of $\tau_{str} = 0.01 \pm 0.01$ at 890 nm. However, there
 515 is some tendency in the results with the Equatorial Zone displaying higher
 516 hazes, although average values of particle density do not differ substantially.
 517 Particle radius seems also to be slightly higher in the low latitudes than
 518 polewards of the region disturbed by the storm.

519 The model excels in fitting the parameters of the tropospheric haze, as
 520 shown in figure 13. In particular, it is very sensitive to its top pressure level,
 521 with the smaller error bars in this study, as it has been already pointed out.
 522 The tropospheric haze top seems to be substantially above the tropopause
 523 level for the EZ, which in any case is not well defined at these latitudes as
 524 analysed from radio occultations (Schinder et al., 2011). At mid-latitudes, it
 525 reaches the 60 mbar level around the latitudes where the mid-latitude jet is
 526 located (García-Melendo et al., 2011).

527 Particle number density is $N_2 = 5 \pm 1 \text{ part/cm}^3$ in the EZ and somewhat
 528 higher at mid-latitudes ($N_2 = 7 \pm 1 \text{ part/cm}^3$), excluding those above 60° ,
 529 which peak at $N_2 = 10 \pm 5 \text{ part/cm}^3$ but with a high dispersion, possibly
 530 due to the limited coverage of the scattering angles at those latitudes which
 531 prevents observing the whole limb-darkening curve from an equatorial orbit.

532 The haze is assumed to decay exponentially above such level with scale
 533 heights lower than those of the gas in Saturn. In the EZ, the scale height is
 534 $H_g/H_p = 10 \pm 5$, while it is about $H_g/H_p = 5 \pm 2$ for the rest of latitudes. Since
 535 the gas scale height in Saturn is about 35km at the 100 mbar pressure level,
 536 this implies a scale height for the haze of $\sim 3.5km$ and $\sim 7km$, respectively.

537 It is possible to integrate the retrieved particle number density from the
 538 top of the atmosphere to retrieve the total optical thickness for the strato-
 539 spheric (at a reference wavelength) and tropospheric (independent of wave-
 540 length by construction) hazes, as shown in figure 14. This obviously re-
 541 sembles the distribution of particle number density but it is very useful for
 542 comparison in previous works (see next section). The stratospheric haze has
 543 a total optical thickness of $\tau_{str} = 0.03 \pm 0.02$ at 890 nm in the EZ. In the
 544 region poleward of the storm, the upper limit seems to be 0.1, except for the
 545 most polar latitudes where the retrievals are much noisier. The total optical
 546 thickness of the tropospheric haze is remarkably constant with latitude, with
 547 averages of $\tau_{trop} = 7 \pm 2$ for both the Equatorial and mid-latitudes. Values
 548 and uncertainties, again, are higher in the polar latitudes, above 60°N.

549 A graphical representation of the vertical distribution of the tropospheric
 550 particles can be found in figure 15. In general terms, higher haze tops are
 551 correlated with lower particle scale heights, i.e. with hazes that end more
 552 abruptly. The latitudes with lower haze tops, conversely, are more extended
 553 with greater scale heights. Latitudes above 60° are the extreme case, al-
 554 though it has already been noted, the retrieved values are substantially nois-
 555 ier and thus less reliable than those at other latitudes.

556 Finally, little or no information can be obtained about the latitudinal

557 distribution of particles at deeper atmospheric levels. There is only a lower
 558 limit to the optical thickness of the bottom cloud ($\tau_{cloud} \geq 10$).

559 5. Discussion

560 5.1. Tropospheric particle phase function

561 The work by Tomasko and Doose (1984) is the only determination of
 562 the phase function for the case of Saturn that can be used to compare our
 563 results. This comparison is presented in table 3, where we show our av-
 564 eraged values for the Equatorial Zone (0° - 15° N), the mid- and sub-polar
 565 latitudes (45° - 70° N) and the global means (0° - 70° N). Focusing on the EZ
 566 values, Tomasko and Doose (1984) results are within our retrieved error bars
 567 for f and backscattering parameter g_2 , while there is a substantial difference
 568 in the forward scattering parameter g_1 . Thus, current results require a more
 569 forward scattering particle phase function than that observed in the late
 570 1970s. This is quite reasonable, since there is no reason why we should ex-
 571 pect a perfect match in mean particle sizes or shapes after one Saturn’s year,
 572 considering also that we are working at different latitudes and wavelengths.

573 Although more limited in phase angle coverage, West et al. (1983) worked
 574 with observations of the Equatorial Zone obtained with the Voyager 2 pho-
 575 topolarimeter from 12° to 68° phase angles. Their resulting values of the
 576 Henyey-Greenstein differ from those presented here in the forward scattering
 577 g_1 , which is lower in their work (0.54 ± 0.11 vs 0.75 ± 0.09) and g_2 (-0.47 ± 0.08
 578 vs -0.33 ± 0.05), somewhat bigger in absolute value. The weighting param-
 579 eter f is also bigger (0.87 ± 0.03 vs 0.79 ± 0.04). In any case, all parameters
 580 are almost within respective error bars, which gives a marginal agreement

581 between both analysis.

582 Although the 2HG phase function is a very useful parameterization of the
583 phase function, it provides little insight into the underlying physics. For this
584 reason, it is very useful to compare the results for the 2HG phase function
585 with a Mie phase function, which assumes sphericity of the particles. How-
586 ever, polarization measurements at Jupiter using Pioneer IPP instrument
587 discarded spherical particles as candidates (Smith & Tomasko, 1984) and it
588 is very likely that the same will be true for Saturn. As discussed for example
589 in West et al. (2009), ice crystals expected at this atmospheric level cannot
590 be modelled using spherical scatterers. Non-spherical particles in the form
591 of aggregates **have** been proposed to explain observations of Jupiter’s polar
592 haze (West and Smith, 1991; Zhang et al., 2013) and could be ubiquitous
593 in the upper atmospheres of the giant planets.

594 It is however possible to use spheroids as a simple approximation to
595 the non-sphericity. With this purpose, we computed the phase function of
596 spheroids with different mean sizes and aspect ratios. The optical properties
597 were obtained from look up tables provided by Dubovik et al. (2006). These
598 use T-matrix calculations for smaller particles combined with ray tracing for
599 the larger particles. The tables have scattering properties at 25 different as-
600 pect ratios between 0.335 and 3.0; 22 real parts of refractive index between
601 1.29 and 1.70; 15 imaginary parts of refractive index between 0.0005 and
602 0.5 and 41 narrow radius bins with size parameters from 0.02 to 626. For
603 imaginary parts of refractive index below 0.0005, there is very little change
604 in optical properties (since at these values, there is close to no absorption)
605 so this value is appropriate for all values below 0.0005. From the simulation

606 results, it is clear that the forward scattering is the best indication of the
 607 particle size, while the backscattering is more influenced by the shape or
 608 aspect ratio.

609 The phase functions for the Equatorial Zone and the mid-latitudes are
 610 shown in figure 16. **At the equator, scattering angles from $\sim 20^\circ$ to**
 611 **$\sim 170^\circ$ are covered** and thus we have a excellent sampling of the phase
 612 function. The forward peak at the EZ is in good agreement with ellipsoids
 613 of mean radius $1 \pm 0.2 \mu\text{m}$, but they do not reproduce well the intermediate
 614 scattering angles even in the best-fitting case of aspect ratio < 0.6 and the fit
 615 is marginal at the best case. We did not find any better fit for EZ particles
 616 using ellipsoids. Yet, ammonia ice crystals have been proposed (West et al.,
 617 2009; Tomasko and Doose, 1984) to be responsible of the observed phase
 618 function. We compare in figure 16 with laboratory data of $10 \mu\text{m}$ ammonia
 619 ice crystals retrieved by Pope et al. (1992). The match is very good and
 620 provides a good indication of the expected size and nature of the tropospheric
 621 particles at the Equatorial Zone.

622 In the case of non-equatorial particles, ammonia ice is not in good agree-
 623 ment with the retrieved phase function at intermediate scattering **angles**.
 624 Ellipsoids, instead, yield an excellent fit again with mean radius $1 \pm 0.2 \mu\text{m}$
 625 and aspect ratio < 0.6 . There is a marginal solution with smaller particles of
 626 mean radius 0.25 ± 0.05 and very elongated (aspect ratio > 0.7). This second
 627 solution, however, clearly misses the scattering at phase angles greater than
 628 100° , so it is not favoured by our results. Such dichotomy would be broken if
 629 we had high phase angle observations for the mid-latitudes of Saturn. In or-
 630 der to understand how this affected our understanding of the phase function

631 at these latitudes, we tried to fit the retrieved values of the phase function
 632 at the observed scattering angles with a different double Henyey-Greenstein
 633 function. It is possible to find another solution consistent at the observed
 634 angles using backscattering parameter $g_2 < -0.9$. This, however, would re-
 635 sult in a extremely strong increase of the phase function at low phase angles
 636 which implies a very intense opposition surge that has not been reported in
 637 Saturn’s atmosphere, even though it has been observed in the rings.

638 A very interesting point is whether or not Equatorial particles can be said
 639 to differ substantially from the particles found at other latitudes, from the
 640 data and retrievals shown in this work. While we have some clues pointing
 641 in that direction (e.g. changes in particle phase function parameters), there
 642 is still a chance that particles at all latitudes are the same since results are
 643 marginally consistent with each other. Results are robust for EZ particles,
 644 but the lack of observations at the forward peak of the phase function makes
 645 results for the other latitudes less reliable. What we see is compatible with
 646 $1\ \mu\text{m}$ ellipsoids moderately elongated, but it could be certainly the case that
 647 ammonia ice crystals were also valid for the mid-latitudes.

648 5.2. Particle distribution

649 This work is the only attempt to date to reproduce the reflectivity of
 650 Saturn at a wide range of phase angles simultaneously since 1979. However,
 651 the results we retrieve from the radiative transfer analysis presented so far
 652 do not differ from our previous understanding of Saturn’s atmosphere. Most
 653 works (Karkoschka and Tomasko, 2005; Pérez-Hoyos et al., 2005; Temma et
 654 al., 2005; Roman et al., 2013) assume a distribution of aerosols in two levels,
 655 as we do in this work. Even though our assumptions may differ from those

656 adopted by others, this basic agreement in the description of the atmosphere
657 allows comparing many atmospheric parameters.

658 Regarding the overall distribution of tropospheric particles, the Equato-
659 rial Zone is in all works the region of the atmosphere displaying higher and
660 thickest hazes, as is for example summarized in figure 1 of Pérez-Hoyos and
661 Sánchez-Lavega (2006a). The Equatorial Zone haze top retrieved here is also
662 located substantially above the tropopause, resembling the results by Roman
663 et al. (2013). While the optical thickness of the Equatorial tropospheric haze
664 is 2-4 times lower than the values retrieved from observations in the 1990s
665 (Pérez-Hoyos and Sánchez-Lavega, 2006a), the values found here are very
666 similar to those found in figure 4 from Roman et al. (2013).

667 At other latitudes, the analogy with the Southern Hemisphere investi-
668 gated by Roman et al. (2013) still holds in both the optical thickness and
669 top pressure, although they also modelled the bottom pressure, here assumed
670 to be fixed at $P_4 = 1\text{bar}$. We find a significant difference for example with
671 Pérez-Hoyos et al. (2005), where the optical thickness at the EZ is 5-10
672 times higher than at the middle latitudes. Something similar happens with
673 Karkoschka and Tomasko (2005), where they found a clear increase in the op-
674 tical thickness of the tropospheric haze towards lower latitudes. Karkoschka
675 and Tomasko (2005) also have tropospheric haze tops at lower levels for most
676 years. It must be noted that these works were based on observations of the
677 Southern Hemisphere (Pérez-Hoyos et al., 2005) at a different epoch, so this
678 can be either a seasonal effect or a difference in the modelling approach.

679 Most of the works cited above used a hard boundary for the tropospheric
680 haze, but in this work we **found that agreement between MT2 and**

681 **MT3 was better using an additional free parameter describing the**
682 **particle scale height.** The work by Tomasko and Doose (1984) also gave a
683 particle scale height at the equatorial latitudes of $H_g/H_p = 3$. This value is
684 within the error bars of our results for the mid-latitudes, but our equatorial
685 hazes in the current epoch have a much more pronounced slope and decay
686 more rapidly (i.e. their scale height is some three times lower than in the
687 Pioneer epoch).

688 Overall, the retrieved values of optical thickness retrieved for the hazes
689 are around the consensus established for Saturn before the Cassini spacecraft
690 were in orbit. As already shown in section 6, total optical thickness for the
691 tropospheric haze is found to be relatively constant with latitude with a
692 mean value of $\tau_{trop} \sim 7$. This could look in contradiction with the commonly
693 assumed paradigm that Equatorial clouds are substantially thicker than at
694 other latitudes. This is based in the lack of thermal emission for example at
695 $5.1 \mu\text{m}$, see figures 7.18 and 7.19 in West et al. (2009). However, it must be
696 noted that we are referring to opacity in the upper bar of the atmosphere
697 and that our model is compatible with a substantial source of cloud opacity
698 below that level.

699 The single scattering albedo at blue wavelengths retrieved here can be
700 compared directly with the values by Pérez-Hoyos et al. (2005). While they
701 cover a greater time span and a different filter selection, their values are
702 clearly lower than ours. Most of they retrievals have $\varpi_0 < 0.9$, and our
703 values are above that threshold for all latitudes. This could be related with
704 the fixed phase function assumed in their work, here found to be somewhat
705 different, which can compensate **for** the differences in the values of the single

706 scattering albedo.

707 Finally, it is certainly very difficult to make any comparison regarding
708 the parameters of the stratospheric haze, given the low sensitivity our anal-
709 ysis has shown to them. Low values of optical thickness and small particle
710 sizes are in good agreement with most retrievals (Pérez-Hoyos et al., 2005;
711 Karkoschka and Tomasko, 2005; Roman et al., 2013); **however it**, is no clear
712 that an increase of particle number density towards the poles can be clearly
713 concluded from the results shown here.

714 Overall, the particle distribution retrieved here is not far from the com-
715 mon picture described in previous works and differences are within retrieval
716 uncertainties in most cases. Although there are many differences in the
717 approach by many teams, it looks like the general distribution of particles
718 around the tropopause level can be confidently retrieved from observations
719 only at low phase angles, which is our most common source of information
720 in the absence of spacecrafts orbiting the planet.

721 *5.3. Dynamical implications*

722 There is a very interesting point that connects the kind of analysis devel-
723 oped here and the atmospheric dynamics we are seeing in the atmosphere.
724 The radiative transfer analysis is the only way we have to determine the ver-
725 tical location of the features used to determine the flows in the atmosphere
726 and the local meteorological phenomena. This implies the analysis of the
727 actual features used for, say, wind tracking, but we can gain some insight
728 by inspecting the contribution functions of each filter through the average
729 atmosphere, shown in figure 17. From this figure we can learn that these con-
730 tribution functions are aerosol dominated and therefore, they seem to sound

731 relatively similar pressure levels in the atmosphere. Figure 17 only shows
 732 MT3 and CB2 contribution functions since they are the two extreme cases,
 733 commonly used for cloud tracking for regions with detected wind shear, as
 734 in García-Melendo et al. (2010, 2011).

735 As noted above, particles at low latitudes have a local peak very high in
 736 the atmosphere and then the contribution function decreases faster than it
 737 does at the middle and sub-polar latitudes. This leaves more space in the
 738 atmosphere for the gas absorption to influence the contribution functions.
 739 Thus, the MT3 contribution function isolines in figure 17 are higher in the
 740 atmosphere and more concentrated, meaning that we are less prone to detect
 741 anything that could be located below the 200 mbar level, while they are
 742 potentially sensitive to levels as high as 10 mbar. By looking through the
 743 CB2 filter, instead, we could potentially detect anything down to the 1 bar
 744 level. It is not only about being able to see through the hazes but also about
 745 having actual atmospheric features at a given altitude level. Moreover, MT2
 746 **and** MT3 are very sensitive to height changes of individual features near
 747 the tropopause while CB2 observations would be insensitive to this kind
 748 of differences. This could help us to understand the vertical wind shears
 749 detected not only in the EZ (Sánchez-Lavega et al., 2003; Vasavada et al.,
 750 2006) but also the smaller shears at the peak jets at other latitudes (García-
 751 Melendo et al., 2011) or their lack of. It is also in close agreement with the
 752 idea that we could be sounding much higher levels in the EZ in the methane
 753 absorption bands than at the continuum and therefore witnessing dynamics
 754 located much higher in the atmosphere (García-Melendo et al., 2010).

755 6. Conclusions

756 In this work, we have analyzed a set of Cassini ISS observations covering
757 blue wavelengths (451nm), two methane bands (centered at 727 and 890
758 nm) and intermediate continuum (750 nm) that cover a wide range of phase
759 angles providing the first chance since 1979 Pioneer 11 analysis to perform
760 a systematic analysis of the particle phase function. Given the wavelengths
761 covered in this work, this phase function is restricted to the upper troposphere
762 levels, which most strongly contribute to the reflected radiation observed in
763 visual wavelengths.

764 We summarize below the most important points of this work and the
765 most important conclusions that can be drawn from it:

- 766 • While the atmosphere was perturbed in 2010 by the uplift of the GWS,
767 this perturbation was restricted to a latitude band between 15° and
768 40° and the rest of the northern hemisphere latitudes show no sign of
769 substantial variation in the reflectivity at the considered filters.
- 770 • The observed reflectivity can be reproduced as a function of wavelength
771 for all the latitudes of interest and emission angles below 80° , by using a
772 relatively simple model for the vertical distribution of particles. Models
773 at higher emission angles depart from observations at MT2 filter, which
774 require **fewer** particles above the tropopause level.
- 775 • Equatorial and mid-latitude hazes have a strongly forward scattering
776 phase function. The phase function at the equator is in good agreement
777 with $10\mu\text{m}$ ammonia ice crystals, **while uncertainties due to lim-**
778 **ited phase coverage and parameter degeneracy prevent strong**

779 constraints of the particle shapes and sizes at mid- and sub-
 780 polar latitudes. These particles may be similar to the equa-
 781 torial particles, but they may also be consistent with 1 μm
 782 ellipsoids with moderate aspect ratios.

- 783 • Global means are similar to previous values provided by Tomasko and
 784 Doose (1984) although there are some differences. Most notably, our
 785 models do not require different phase function parameters for blue
 786 wavelengths, which can be reproduced with the same parameters as
 787 in the near infrared wavelengths. The main difference in the Equato-
 788 rial phase function is that Tomasko and Doose (1984) has lower values
 789 of the forward scattering parameter, beyond the retrieval uncertainties.
- 790 • The overall integrated optical thickness and haze top values for the
 791 tropospheric haze are in close agreement with previous results regarding
 792 different seasons of the Saturnian year.
- 793 • Analysis of the contribution function for the filters commonly used for
 794 cloud tracking and most extremely sounding (MT3 and CB2), show
 795 that both are aerosol dominated. However, MT3 sounding levels are
 796 restricted from ~ 10 mbar down to ~ 200 mbar, while CB2 is able to
 797 sound well past the 1 bar level. This puts into context the detection of
 798 vertical wind shears for the Equator and is consistent with two separate
 799 dynamical levels being seen at some latitudes.

800 Now that we are approaching the end of the Cassini mission in 2017, it
 801 would be useful that analysis like the present one here could be undertaken for
 802 other latitudes and time spans, although it should be noted that both phase

803 angle coverage and stability of the atmosphere at the latitudes of interest
804 must be present.

805 **Acknowledgements**

806 We gratefully acknowledge the work of the Cassini ISS team that made
807 the data available. This work was supported by the Spanish MICIIN project
808 and AYA2012-36666 with FEDER support, Grupos Gobierno Vasco IT765-
809 13, and UPV/EHU UFI11/55. S.P.-H. acknowledges support from the Jose
810 Castillejo Program funded by Ministerio de Educación, Cultura y Deporte,
811 Programa Nacional de Movilidad de Recursos Humanos del Plan Nacional
812 de I-D+i 2008-2011. This work has benefited from the comments of Dr. R.
813 West and Dr. M. Roman during the review process.

814 **References**

- 815 Dubovik, O., A. Sinyuk, T. Lapyonok, B.N. Holben, M. Mishchenko, P. Yang,
816 T.F. Eck, H. Volten, O. Muñoz, B. Veihelmann, W.J. van der Zande, J.-F.
817 Leon, M. Sorokin, and I. Slutsker, 2006: Application of spheroid models to
818 account for aerosol particle nonsphericity in remote sensing of desert dust.
819 J. Geophys. Res., 111, D11208.
- 820 Fischer, G. et al., 2011. A giant thunderstorm on Saturn. *Nature* 475, 7577.
- 821 Fletcher, L.N., G.S. Orton, N.A. Teanby, P.G.J. Irwin, G.L. Bjoraker, 2009.
822 Methane and its isotopologues on Saturn from Cassini/CIRS observations.
823 *Icarus* 199, pp. 351367.
- 824 Fletcher, L.N. et al., 2011. Thermal structure and dynamics of Saturn's
825 northern springtime disturbance. *Science* 332, 14131417.
- 826 Fletcher, L.N., K.H. Baines, T.W. Momary, A.P. Showman, P.G.J. Irwin, G.
827 S. Orton, M. Roos-Serote, and C. Merlet, 2011. Saturn's tropospheric com-
828 position and clouds from Cassini/VIMS 4.65.1 m nightside spectroscopy.
829 *Icarus* 214, 510-533.
- 830 García-Melendo, E., A. Sánchez-Lavega, J. Legarreta, S. Pérez-Hoyos and
831 R. Hueso, 2010. A strong high altitude narrow jet detected at Saturn's
832 equator. *Geophysical Research Letters* 37, L22204.
- 833 García-Melendo, E., S. Pérez-Hoyos, A. Sánchez-Lavega and R. Hueso, 2011.
834 Saturn's zonal wind profile in 2004-2009 from Cassini ISS images and its
835 long-term variability. *Icarus* 215, 62-74.

836 Hansen, J.E., Travis, L.D., 1974. Light scattering in planetary atmospheres.
837 Space Sci. Rev. 16, 527610.

838 Henyey, L.C., Greenstein, J.L., 1941. Diffuse radiation in the Galaxy. Astro-
839 phys. J. 93, 7083.

840 Hueso, R. J. Legarreta, J.F. Rojas, J. Peralta, S. Prez-Hoyos, T. del Ro-
841 Gaztelurrutia and A. Snchez-Lavega, 2010. The Planetary Laboratory for
842 Image Analysis (PLIA). Advances in Space Research, 46, 1120-1138.

843 Irwin, P.G.J., N.A. Teanby, R. de Kok, L.N. Fletcher, C.J.A. Howett, C.C.C.
844 Tsang, C.F. Wilson, S.B. Calcutt, C.A. Nixon, P.D. Parrish, 2008. The
845 NEMESIS planetary atmosphere radiative transfer and retrieval tool. Jour-
846 nal of Quantitative Spectroscopy and Radiative Transfer 109, 1136-1150.

847 Irwin, P.G.J., L.N. Fletcher, P.L. Read, D. Tice, I. de Pater, G.S. Orton, N.A.
848 Teanby and G.R. Davis, 2015. Spectral analysis of Uranus' 2014 bright
849 storm with VLT/SINFONI. Icarus 264, 72-89.

850 Karkoschka, E., Tomasko, M.G., 2005. Saturn's vertical and latitudinal cloud
851 structure 19912004 from HST imaging in 30 filters. Icarus 179, 195221.

852 Karkoschka, E., Tomasko, M.G., 2010. Methane absorption coefficients for
853 the Jovian planets from laboratory, Huygens, and HST data. Icarus 205,
854 674694.

855 de Kleer, K., S. Luszcz-Cook, I. de Pater, M. Adamkovics, H.B. Ham-
856 mel, 2015. Clouds and aerosols in Uranus: radiative transfer modeling
857 of spatially-resolved near-infrared Keck spectra. Icarus 256, 120-137.

- 858 Lindal, G.F., Sweetnam, D.N., Eshleman, V.R., 1985. The atmosphere of
859 Saturnian analysis of the Voyager radio occultation measurements. *Astron.*
860 *J.* 90, 11361146
- 861 Liou, K.N., 1992. *Radiation and Cloud Processes in the Atmosphere*. Oxford
862 Univ. Press, New York.
- 863 Martonchik, J.V., Orton, G.S., Appleby, J.F., 1984. Optical properties of
864 NH₃ ice from the far infrared to the near ultraviolet. *Appl. Optics* 23,541-
865 547
- 866 Nelder, J.A. & R. Mead, 1965. A Simplex method for function minimization.
867 *The Computer Journal* 7, 308-313.
- 868 Pérez-Hoyos, S., Sánchez-Lavega, A., French, R.G., Rojas, J.F., 2005. Sat-
869 urn's cloud structure and temporal evolution from ten years of Hubble
870 space telescope images (1994-2003). *Icarus* 176, 155174.
- 871 Pérez-Hoyos, S., Sánchez-Lavega, A., 2006a. On the vertical wind shear of
872 Saturn's Equatorial jet at cloud level. *Icarus* 180, 161175.
- 873 Pérez-Hoyos, S., Sánchez-Lavega, A., 2006b. Solar flux in Saturn's atmo-
874 sphere: Penetration and heating rates in the aerosol and cloud layers.
875 *Icarus* 180, 368 378.
- 876 Pérez-Hoyos, S., Sánchez-Lavega, A. and R. G. French 2006c. Short-term
877 changes in the belt/zone structure of Saturns Southern Hemisphere (1996-
878 2004), *Astronomy & Astrophysics*, 460, 641-645.

879 Pérez-Hoyos, S., Sanz-Requena, J.F., Barrado-Izagirre, N., Rojas, J.F.,
880 Sánchez-Lavega, A., 2012. The 2009-10 fade of Jupiter's South Equato-
881 rial Belt: Vertical cloud structure models and zonal winds from visible
882 imaging. *Icarus* 217, 256271.

883 Pope, S.K., M.G. Tomasko, M.S. Williams et al., 1992. Clouds of ammonia
884 ice: Laboratory measurements of single-scattering properties. *Icarus* 100,
885 203-220.

886 Porco, C.C. et al., 2004. Cassini Imaging Science: Instrument characteristics
887 and anticipated scientific investigations at Saturn. *Space Sci. Rev.* 115,
888 363497.

889 del Río-Gaztelurrutia, T., Legarreta, J., Hueso, R., Pérez-Hoyos, S., Sánchez-
890 Lavega, A., 2010. A long-lived cyclone in Saturn's atmosphere: Observa-
891 tions and models. *Icarus* 209, 665681.

892 Rodgers, C.D., 2000. Inverse methods for atmospheric sounding. Theory and
893 practice. World Scientific, London.

894 Roman, M.T., D. Banfield and P.J. Gierasch (2013). Saturn's cloud structure
895 from Cassini ISS. *Icarus* 225, 93-110.

896 Sánchez-Lavega, A., 2011. An Introduction to Planetary Atmospheres. CRC
897 Press, Boca Raton, FL, USA.

898 Sánchez-Lavega, A., Colas, F., Lecacheux, J., Laques, P., Miyazaki, I.,
899 Parker, D., 1991. The great white spot and disturbances in Saturn's Equa-
900 torial atmosphere during 1990. *Nature* 353, 397401.

901 Sánchez Lavega, A., J. Lecacheux, F. Colas, P. Laques, 1993. Temporal be-
 902 havior of cloud morphologies and motions in Saturn's atmosphere, Journal
 903 of Geophysical Research, 98 (E10), 18857 - 18872.

904 Sánchez-Lavega, A., S. Pérez-Hoyos, J. F. Rojas, R. Hueso and R. G. French,
 905 2003. A strong decrease in Saturn's equatorial jet at cloud level. Nature,
 906 423, 623-625.

907 Sánchez-Lavega, A., Pérez-Hoyos, S., Hueso, R., 2004. Clouds in planetary
 908 atmospheres: A useful application of the Clausius-Clapeyron equation. Am.
 909 J. Phys. 72, 767774. doi:10.1119/1.1645279.

910 Sánchez-Lavega, A., Hueso, R., Pérez-Hoyos, S., 2007. The three-dimensional
 911 structure of Saturn's Equatorial jet at cloud level. Icarus 187, 510519.

912 Sánchez-Lavega, A. et al., 2011. Deep winds beneath Saturn's upper clouds
 913 from a seasonal long-lived planetary-scale storm. Nature 475, 7174.

914 Sánchez-Lavega, A., T. del Río-Gaztelurrutia, M. Delcroix, J. J. Legarreta,
 915 J. M. Gómez-Forrellad, R. Hueso, E. García-Melendo, S. Pérez-Hoyos, D.
 916 Barrado-Navascus, Jorge Lillo, 2012. Ground-based Observations of the
 917 Long-term Evolution and Death of Saturn's 2010 Great White Spot, Icarus,
 918 220, 561-576.

919 Sanz-Requena, J.F., S. Pérez-Hoyos, A. Sánchez-Lavega, T. del Río-
 920 Gaztelurrutia, D. Barrado-Navascués, F. Colas, J. Lecacheux, D. Parker,
 921 2012. Cloud structure of Saturn's 2010 storm from ground-based visual
 922 imaging. Icarus 219, 142-149.

923 Sayanagi, K.M., U.A. Dyudina, S.P. Ewald, G. Fischer, A.P. Ingersoll, W.S.
924 Kurth, G.D. Muro, C.C. Porco and R.A. West, 2013. Dynamics of Saturns
925 great storm of 20102011 from Cassini ISS and RPWS. *Icarus* 223, 460-478.

926 Schinder, P. J., F. M. Flasar, E. A. Marouf, R. G. French, C. A. McGhee, A.
927 J. Kliore, N. J. Rappaport, E. Barbinis, D. Fleischman, and A. Anabtawi.
928 Saturn's equatorial oscillation: Evidence of descending thermal structure
929 from Cassini radio occultations, *Geophys. Res. Lett.* 38, L08205.

930 Smith, P.H. and M.G. Tomasko, 1984. Photometry and polarimetry of
931 Jupiter at large phase angles. II. Polarimetry of the South Tropical Zone,
932 South Equatorial Belt, and the Polar Regions from the Pioneer 10 and 11
933 missions. *Icarus* 58, 35-73.

934 Sromovsky, L.A., K.H. Baines and P.M. Fry, 2013. Saturns Great Storm of
935 2010-2011: Evidence for ammonia and water ices from analysis of VIMS
936 spectra. *Icarus* 226, 402-418.

937 Temma, T., Chanover, N.J., Simon-Miller, A.A., Glenar, D.A., Hillman, J.J.,
938 Kuehn, D.M., 2005. Vertical structure modeling of Saturn's Equatorial
939 region using high spectral resolution imaging. *Icarus* 175, 464-489

940 Tomasko, M.G., Dose, L.R., 1984. Polarimetry and photometry of Saturn
941 from pioneer 11: Observations and constraints on the distribution and
942 properties of cloud and aerosol particles. *Icarus* 58, 134.

943 Tomasko, M.G., West, R.A., Orton, G.S., Tejfel, V.G., 1984. Cloud and
944 aerosols in Saturns atmosphere. In: Gehrels, T., Matthews, M.S. (Eds.),
945 Saturn. Univ. of Arizona Press, Tucson, AZ, pp. 150-194.

946 Tomasko, M.G. and L.R. Dose, 1985. Clouds and aerosols on Saturn. In:
947 ESA The Atmospheres of Saturn and Titan p 53-61 (SEE N86-28849 19-
948 88).

949 Van de Hulst, H.C., 1957. Light scattering by small particles. Courier Dover
950 Publications, New York.

951 Vasavada, A.R. et al., 2006. Cassini imaging of Saturn: Southern hemisphere
952 winds and vortices. *J. Geophys. Res.* 111, E05004.

953 West, R.A., 1983. Spatially resolved methane band photometry of Saturn:
954 II. Cloud structure models at four latitudes. *Icarus* 53, 301-309.

955 West, R.A., M. Sato, H. Hart, A.L. Lane, C.W. Hord, K.E. Simmons, L.W.
956 Esposito, D.L. Coffeen, and R.B. Pomphrey, 1983. Photometry and po-
957 larimetry of Saturn at 2640 and 7500 Å. *J. Geophys. Res.*, 88, 8679-8697.

958 West, R. A., and P. H. Smith 1991. Evidence for aggregate particles in the
959 atmospheres of Titan and Jupiter. *Icarus* 90, 330-333.

960 West, R.A., Baines, K.H., Karkoschka, E., Sanchez-Lavega, A., 2009. Clouds
961 and aerosols in Saturn's atmosphere. In: Dougherty, M.K., Esposito, L.W.,
962 Krimigis, S.M. (Eds.), *Saturn from Cassini-Huygens*. Springer, New York,
963 pp. 113-159.

964 West, Robert; Knowles, Benjamin; Birath, Emma; Charnoz, Sebastien; Di
965 Nino, Daiana; Hedman, Matthew; Helfenstein, Paul; McEwen, Alfred;
966 Perry, Jason; Porco, Carolyn; Salmon, Julien; Throop, Henry; Wilson,
967 Daren, 2010. In-flight calibration of the Cassini imaging science sub-system
968 cameras. *Planetary and Space Science* 58, 1475-1488.

⁹⁶⁹ Zhang, X., R.A. West, D. Banfield and Y.L. Yung, 2013. Stratospheric
⁹⁷⁰ aerosols on Jupiter from Cassini observations. *Icarus* 226, 159-171.

Table 1: Summary of the Cassini ISS observations.

Date	B	B'	α
2010-12-05	-0.02	7.21	80.2
2010-12-23	-0.02	7.46	60.8
2010-12-24	-0.03	7.48	71.2
2011-01-06	-0.07	7.66	113.3
2011-01-09	-0.07	7.71	146.9
2011-01-15	0.26	7.80	78.0
2011-01-21	0.31	7.88	95.4
2011-03-07	0.37	8.52	84.8
2011-03-19	0.17	8.69	157.7
2011-04-22	0.29	9.16	57.6
2011-05-03	0.37	9.31	86.3
2011-06-14	0.38	9.90	94.8
2011-07-14	0.10	10.31	20.5
2011-08-03	0.03	10.58	12.1
2011-08-06	0.16	10.63	28.2
2011-09-06	0.30	11.05	53.6
2011-11-30	0.20	12.18	41.8
2011-12-31	-0.79	12.58	79.4

B : sub-spacecraft planetocentric latitude

B' : sub-solar planetocentric latitude

α : phase angle

Table 2: Model atmosphere parameters.

Layer	Parameter	Type	Value
Stratospheric Haze	P_1	Free	0.1-100 mbar
	P_2	Fixed	100 mbar
	N_1	Free	$10^{-3} - 10^1 \text{ part}/\text{cm}^3$
	H_1	Free	$10^{-3} - 10^3 H_g/H_p$
	m_r	Fixed	Ammonia ice
	m_i	Fixed	Ammonia ice
	r_g	Free	$0.05 - 0.5 \mu\text{m}$
	σ_g	Fixed	0.1
Tropospheric Haze	P_3	Free	10-200 mbar
	P_4	Fixed	1 bar
	N_2	Free	$10^{-1} - 10^2 \text{ part}/\text{cm}^3$
	H_2	Free	$10^{-3} - 10^3 H_g/H_p$
	$\varpi_{02} \text{ (BL1)}$	Free	0.5 - 1.0
	$\varpi_{02} \text{ (IR)}$	Fixed	0.995
	σ_2	Fixed	$\pi \times 10^{-8} \text{cm}^2$
	f	Free	0.5 - 0.99
Bottom Cloud	g_1	Free	0.5 - 0.99
	g_2	Free	-0.05 - -0.5
	P_5	Fixed	1.0 bar
	P_6	Fixed	1.4 bar
	N_3	Free	$10^0 - 10^3 \text{ part}/\text{cm}^3$
	σ_3	Fixed	$\pi \times 10^{-6} \text{cm}^2$
	ϖ_{03}	Fixed	0.995

Table 3: Comparison of 2HG parameters with Tomasko and Doose (1984)

Latitude	f	g ₁	g ₂	Source
0-15N	0.79±0.04	0.75±0.09	-0.33±0.05	All wavelengths - This work
40-70N	0.88±0.04	0.83±0.04	-0.31±0.07	All wavelengths - This work
0-70N	0.85±0.06	0.81±0.07	-0.31±0.07	All wavelengths - This work
7-11S	0.763	0.620	-0.294	R - T&D (1984)
15-17S	0.768	0.603	-0.302	R - T&D (1984)
7-11S	0.920	0.710	-0.317	B - T&D (1984)
15-17S	0.764	0.870	-0.116	B - T&D (1984)

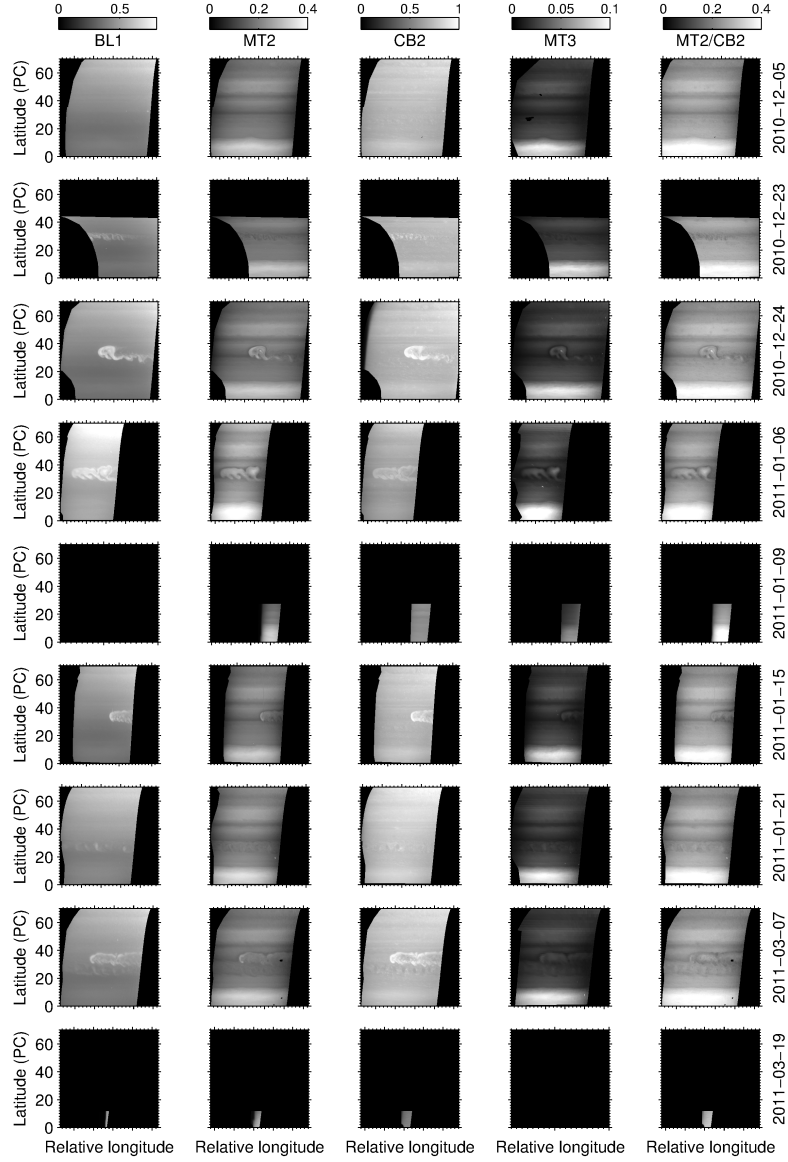


Figure 1: Cylindrically projected maps for the three selected filters and MT2/CB2 ratio dates before March, 2011. All maps are oversampled to a resolution of 0.1° per pixel. Each map covers 100° in longitude and spans from 0° to 70° North. All maps are calibrated in absolute reflectivity and Lambert corrected for limb-darkening. The reflectivity has been scaled in the cases with most extreme phase angles (January 9 and March 19) to fit the same grayscale levels.

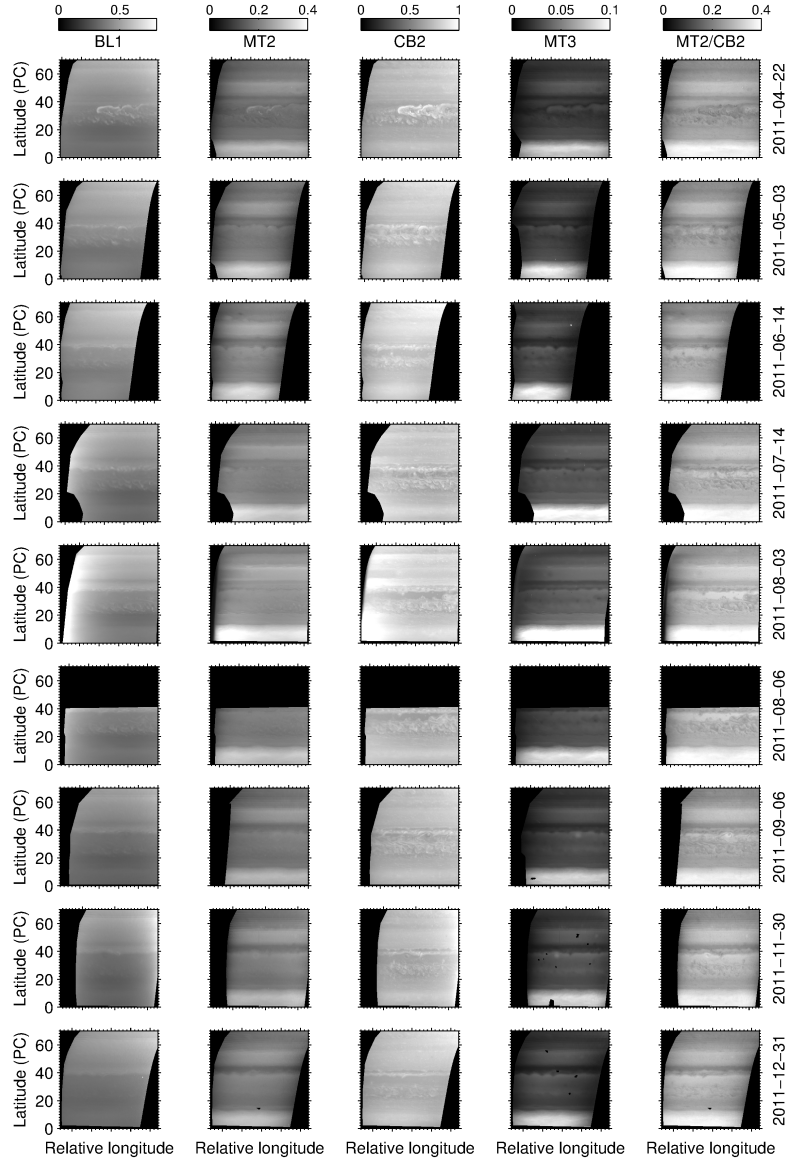


Figure 2: Same as figure 1 for the rest of dates.

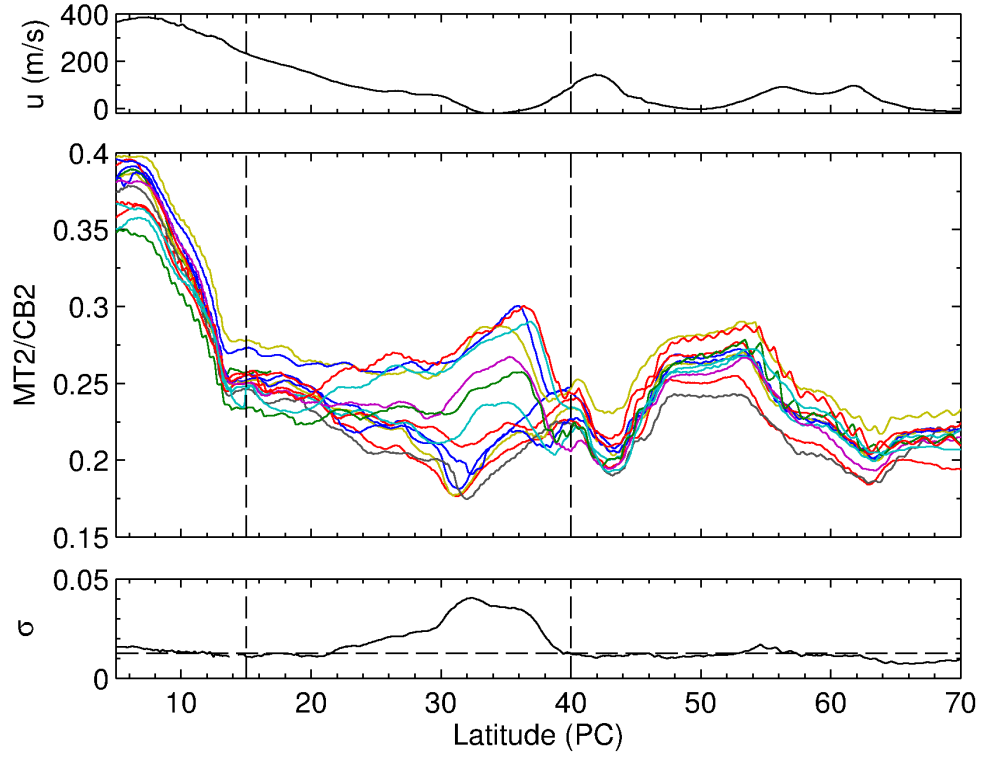


Figure 3: (up) Zonal wind speeds u as a function of latitude from García-Melendo et al. (2011). (middle) Zonal means of the MT2/CB2 ratio for all dates with phase angles from 20° to 100° . (bottom) Standard deviation σ of all scans as a function of latitude. The horizontal dashed line shows the average of σ for the region analyzed in this work. The area between the vertical dashed lines indicates the excluded region.

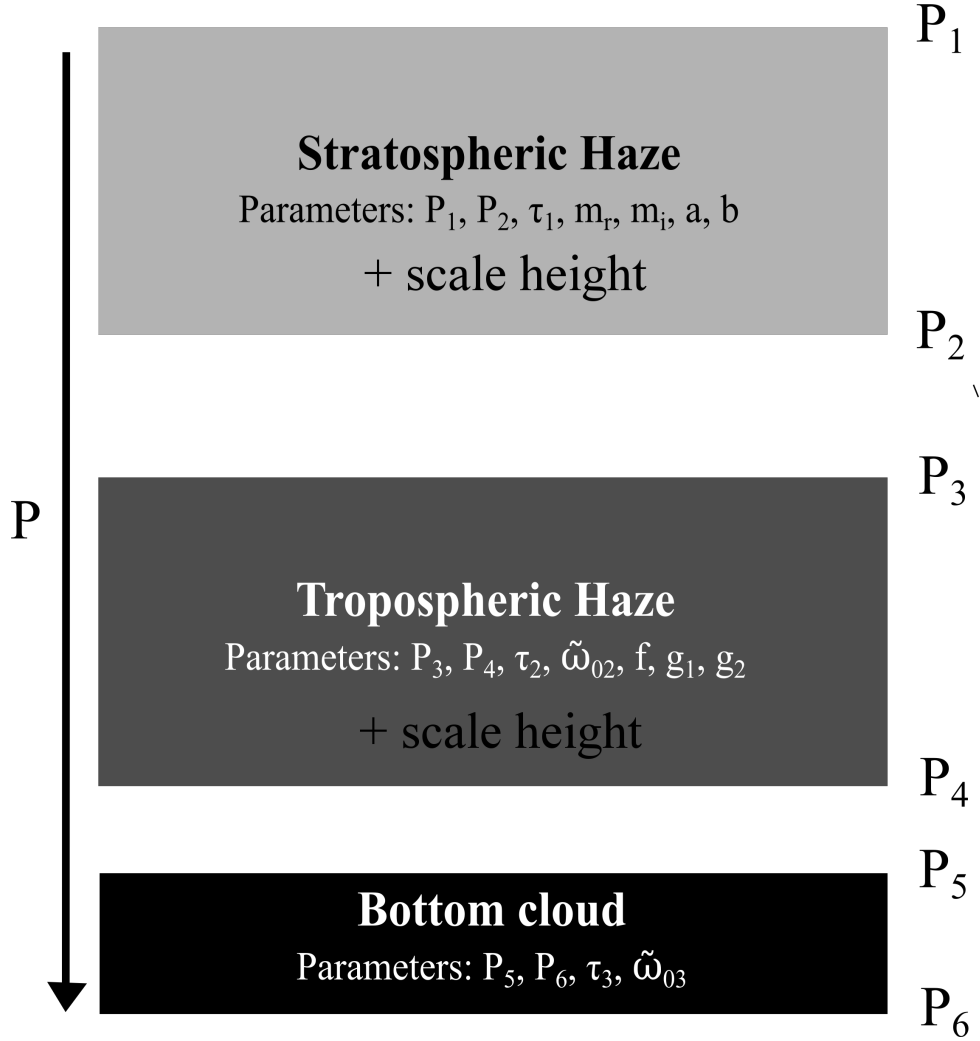


Figure 4: Scheme of the vertical cloud structure model used in this work and the parameters required to define it. All haze and cloud layers are assumed to have constant particle number density between boundary pressure levels. The particle number densities of the hazes decay exponentially above the top level with the corresponding scale height.

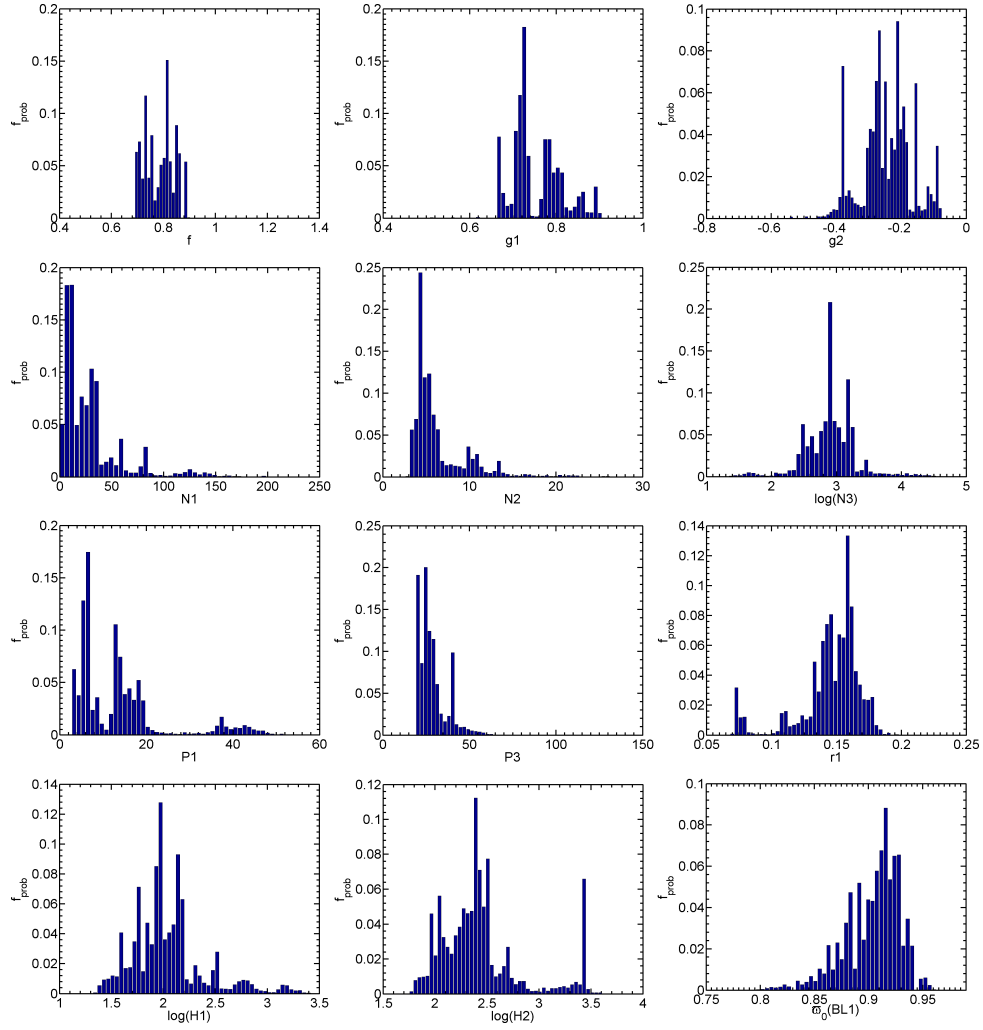


Figure 5: Histograms showing the relative frequency of each model parameter weighted by the probability of the model of being exact as explained in the text. Higher values of relative frequency implies a greater probability of this value to be correct.

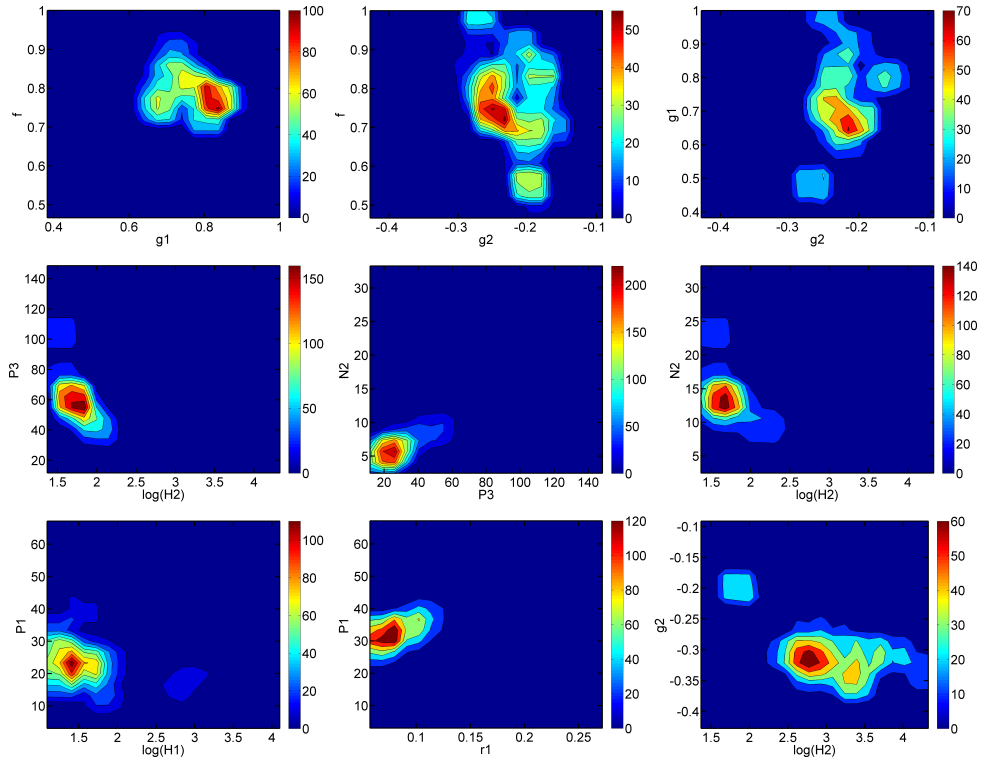


Figure 6: Density of models (weighted by the probability) for some combinations of the free parameters. Higher values in a given region of the free parameter space imply a bigger probability of the solution to be there.

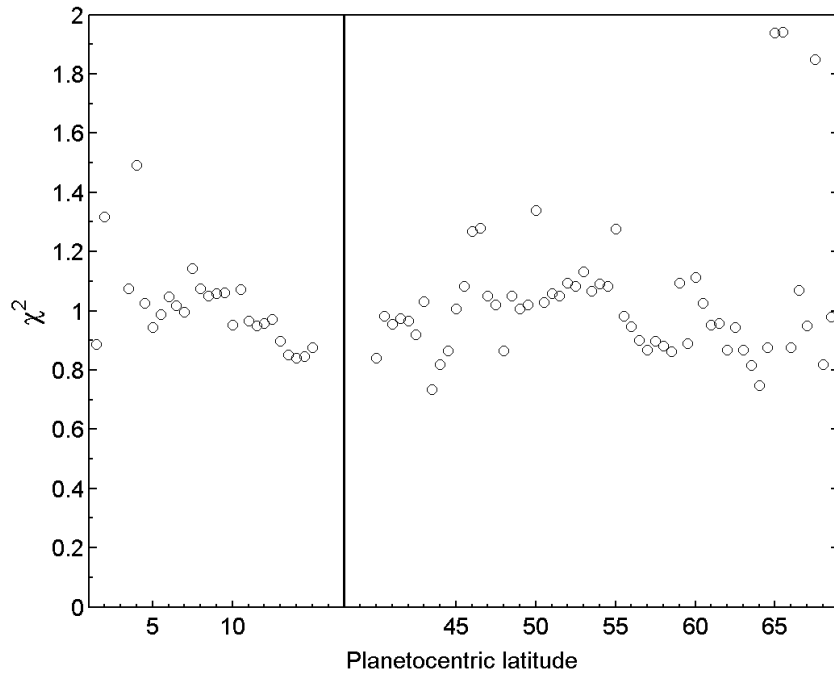


Figure 7: Reduced χ^2 (mean for every point and wavelength) for all latitudes.

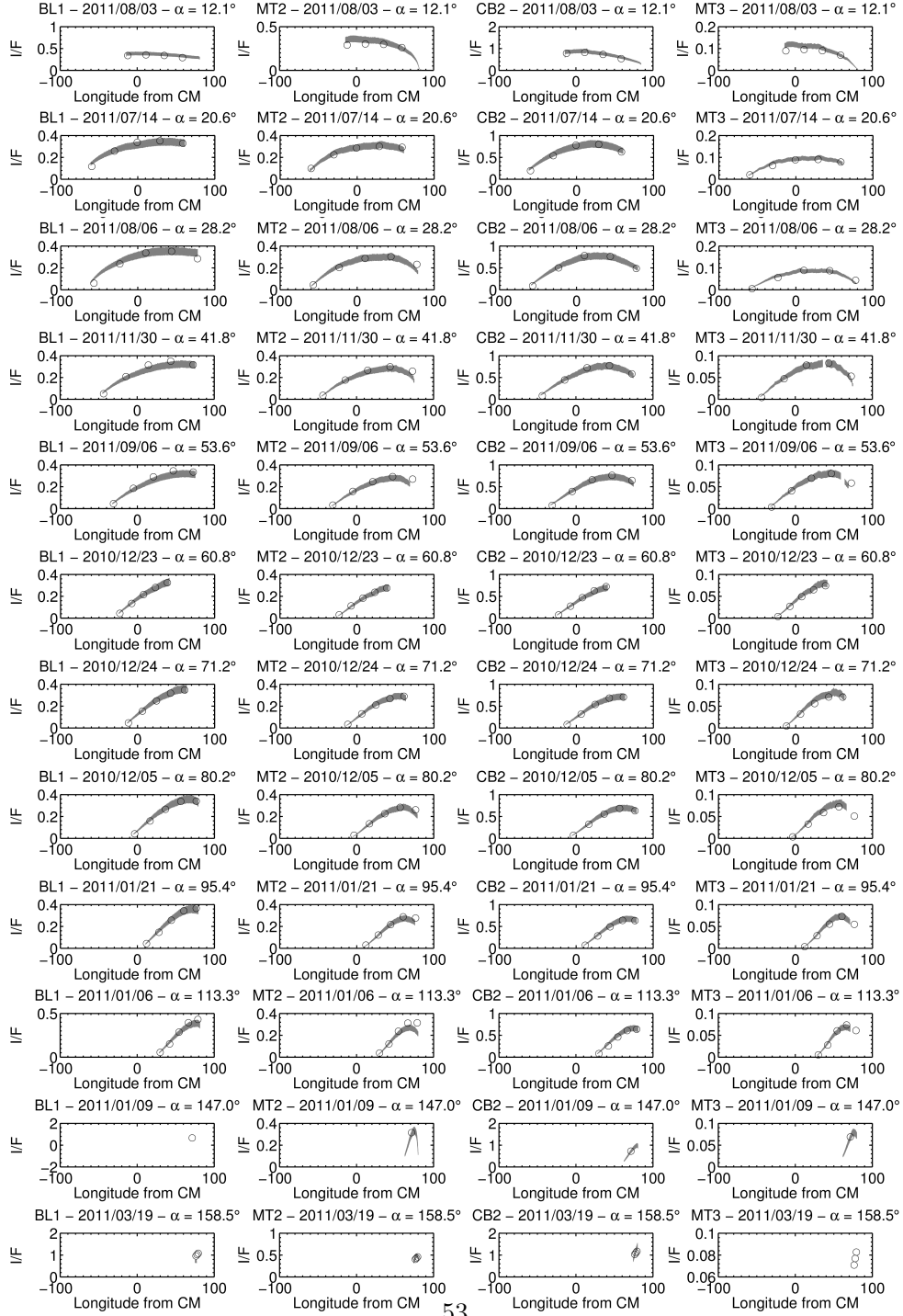


Figure 8: Comparison between observed reflectivity (grey) and best-fitting models (black circles) for some selected dates at 5°N. Dates have been chosen to cover the whole phase angle range at similar intervals and they are shown in increasing values of α from top to bottom.

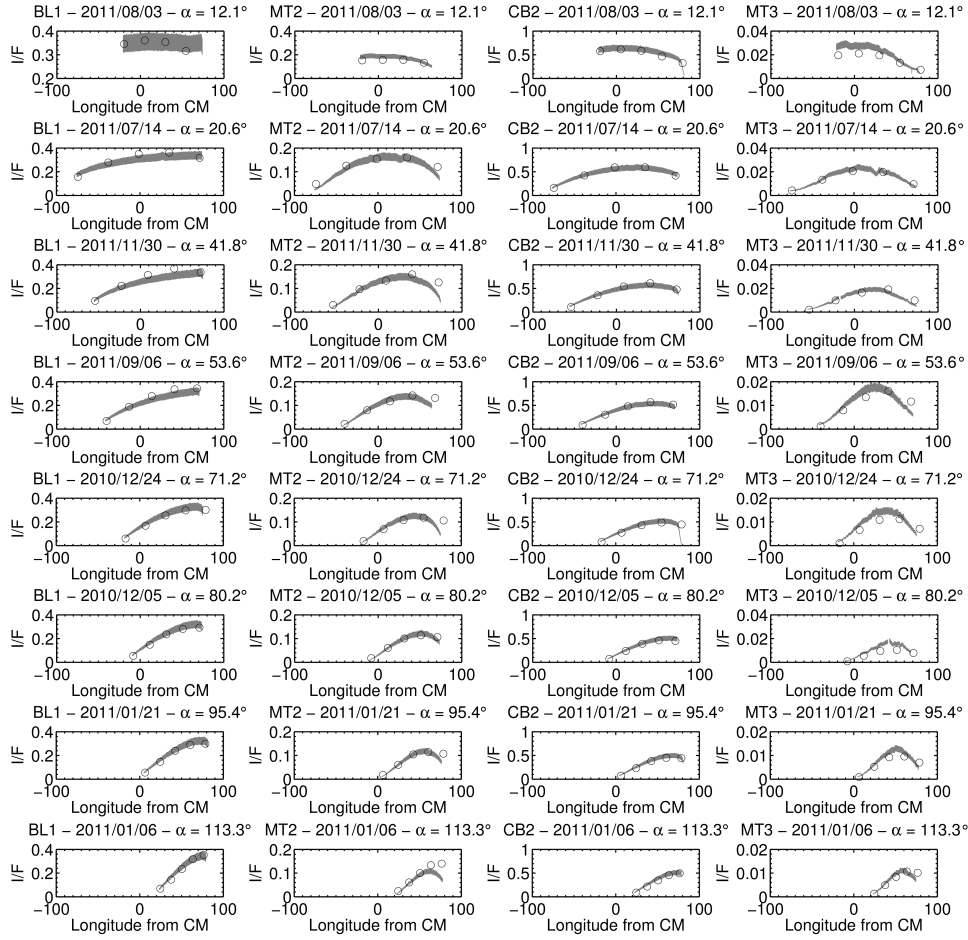


Figure 9: Same as figure 8 but for 45°N . Note the more limited phase angle coverage for this case.

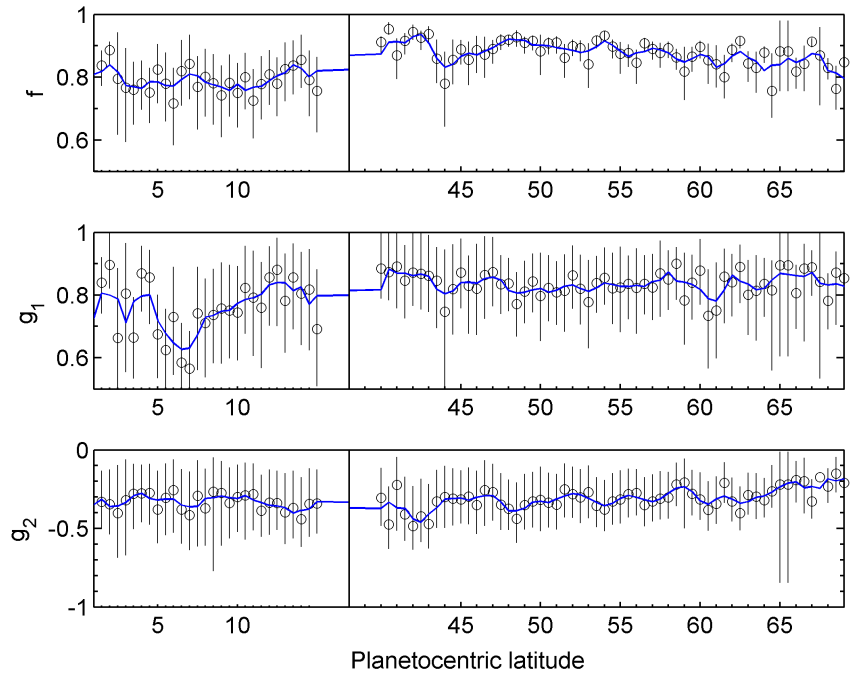


Figure 10: Optimal values of 2HG parameters as a function of latitude (circles) and estimated error bars. The solid line is a running average smooth in 2° latitude bins. These values are valid for all the wavelengths covered in this work, as explained in the text.

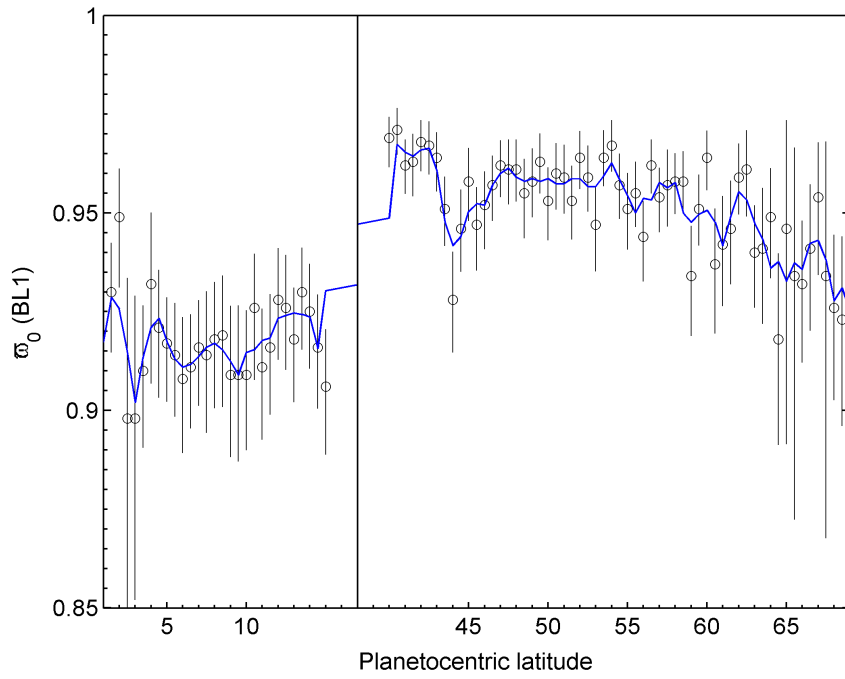


Figure 11: Single scattering albedo ϖ_0 at blue wavelengths (circles) as a function of latitude. The solid line is a running average smooth in 2° latitude bins.

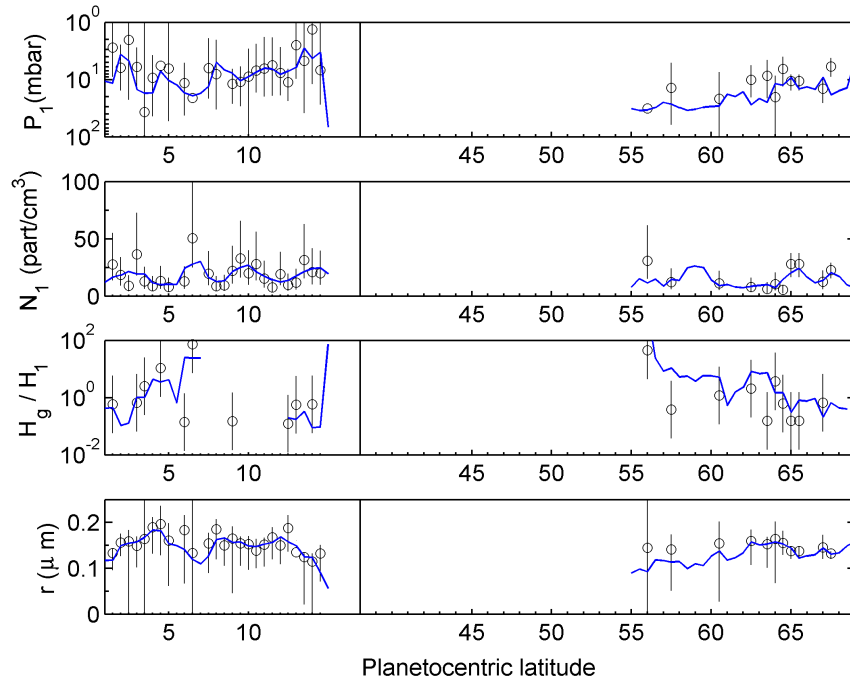


Figure 12: Best-fitting parameters for the stratospheric haze (circles). Results are shown only for the latitudes with integrated optical thickness $\tau_{str} > 0.01$. The solid line is a running average smooth in 2° latitude bins. Scale height is given in terms of the gas scale height H_g .

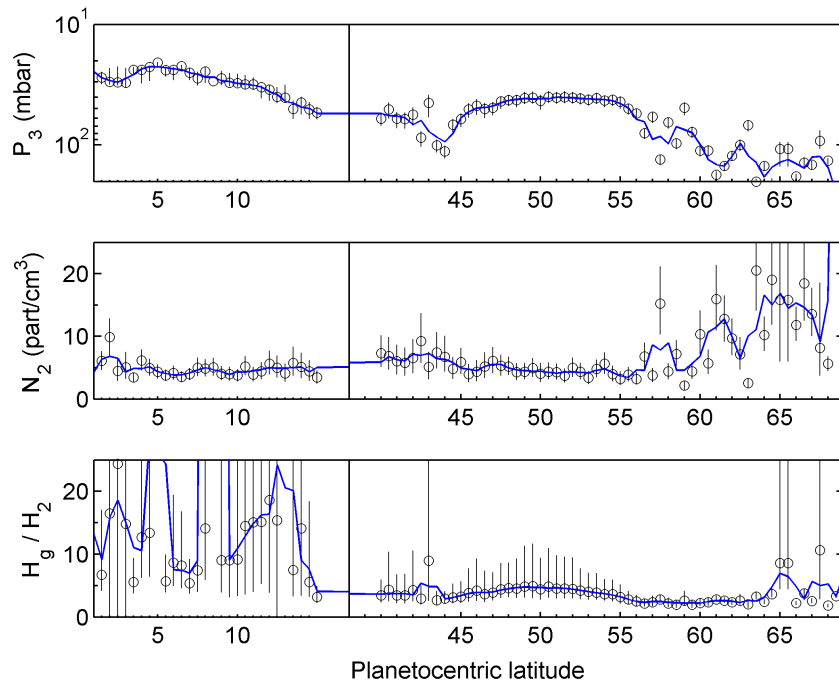


Figure 13: Best-fitting parameters for the tropospheric haze (circles). The solid line is a running average smooth in 2° latitude bins. Scale height is given in terms of the gas scale height H_g .

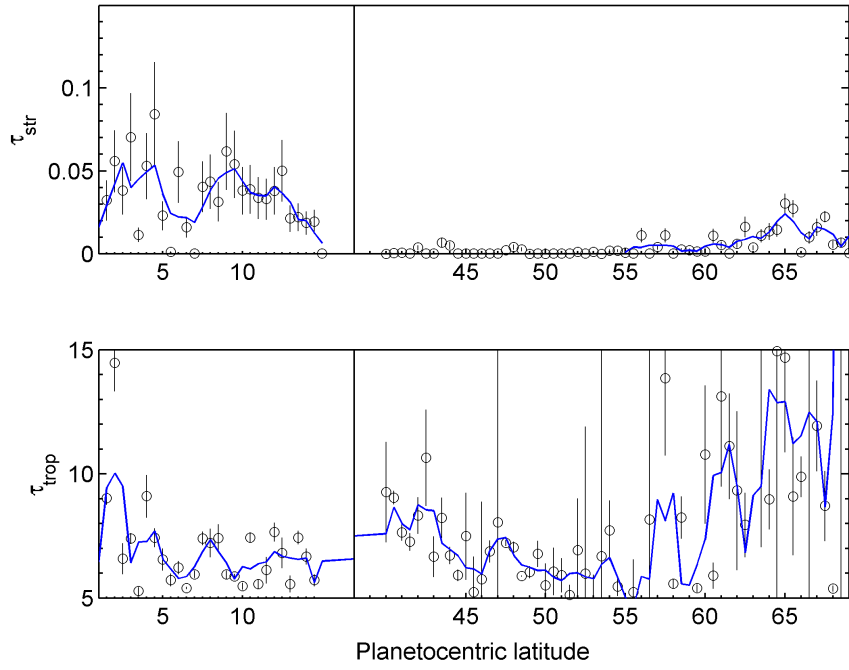


Figure 14: Total optical thickness of the stratospheric (top) and tropospheric (bottom) hazes. As defined in the text, the first provides the total optical thickness above $P_2 = 100$ mbar caused by stratospheric particles and the second the total optical thickness above $P_4 = 1$ bar caused by the tropospheric particles.

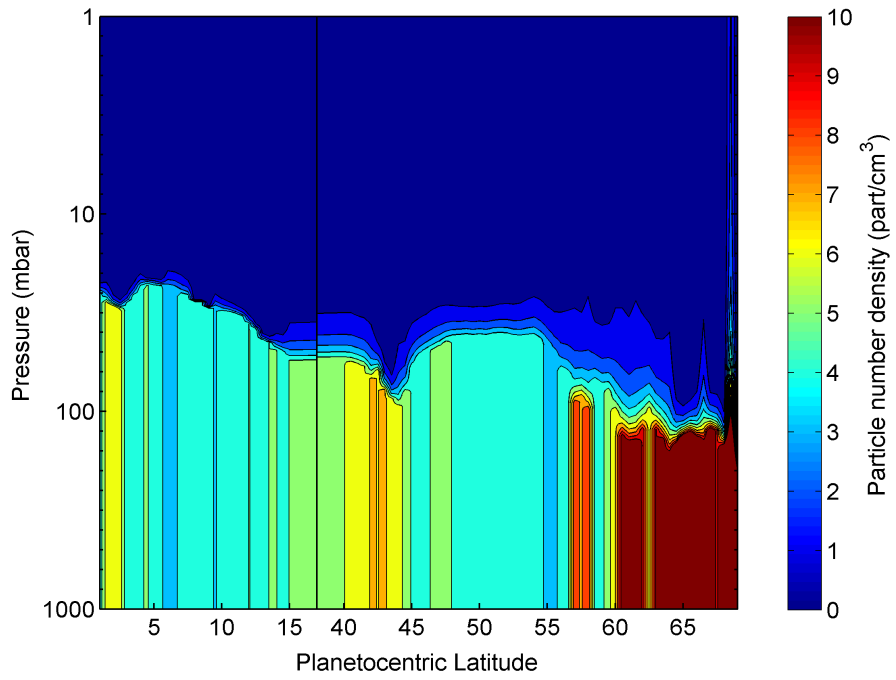


Figure 15: Tropospheric particle number density as a function of latitude and pressure. This plot has been constructed using the smoothed version of the retrievals shown in the previous figures, using 2° latitude bins. Stratospheric aerosols are not shown in this figure. Note that number density was forced to be constant between limiting pressures P_3 and $P_4 = 1$ bar by model construction.

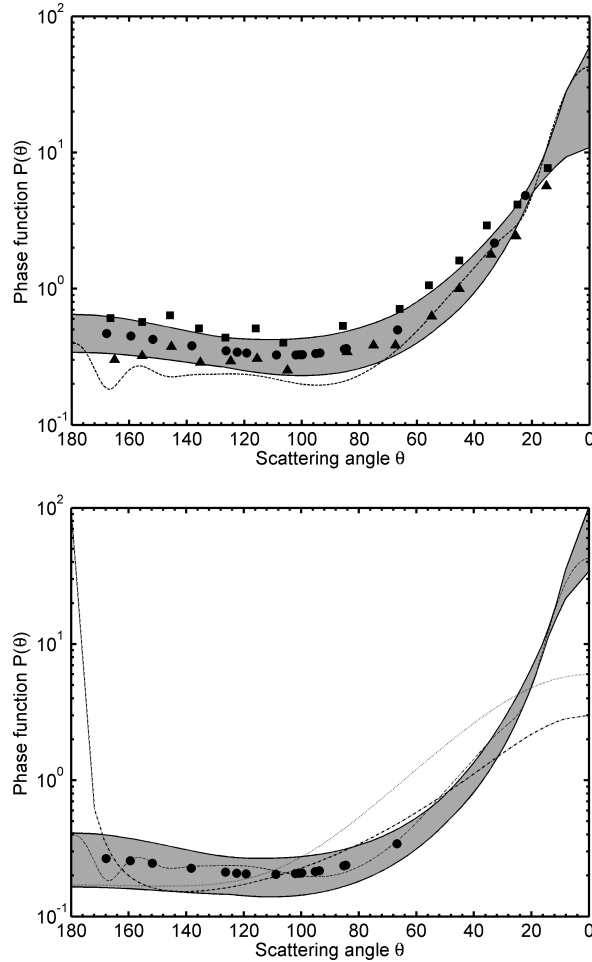


Figure 16: (top) Phase function of the EZ particles at the actual phase angles covered in this work with the nominal values of table 3 (circles) and extrapolated to all possible scattering angles with the retrieved error bars (grey area). This is compared with the phase function of $10\ \mu\text{m}$ ice crystals grown in laboratory (Pope et al., 1992) at blue (triangles) and red (squares) wavelengths. Dashed line is used for spheroids of $1\ \mu\text{m}$ mean radius and aspect ratio of $2/3$. (bottom) Same for the non equatorial particles. Dotted line is used for particles $0.25\ \mu\text{m}$ mean radius and aspect ratio of $1/3$, marginally compatible at intermediate scattering angles. The dashed-dotted line is used for an alternative double Henyey-Greenstein phase function ($f = 0.5, g_1 = 0.5, g_2 = -0.95$) compatible with phase function values at the observed scattering angles. Note that this phase function implies a heavy opposition surge. A scattering angle of 0° means forward scattering, while 180° means backward scattering.

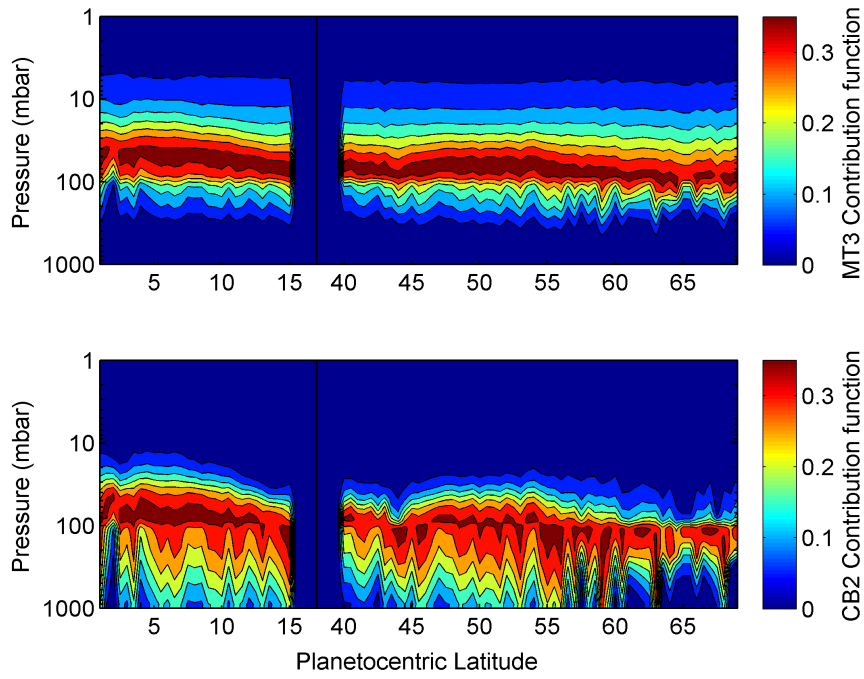


Figure 17: Contribution function for MT3 (top) and CB2 (bottom). These include gas absorption by CH_4 and particle scattering using the values retrieved in the previous sections. Please note that discontinuities are produced by the particle distribution in the atmospheric model.